

A New Approach To Inverting Backscatter and Scatter from Photon-Limited Lidar Observations

Willem J. Marais^{1,2,†}, Robert E. Holz², Yu Hen Hu¹, Ralph E. Kuehn², Edwin E. Eloranta³, and Rebecca M. Willett¹

¹Department of Electrical and Computer Engineering (ECE), University of Wisconsin-Madison, Madison, Wisconsin, USA

²Cooperative Institute for Meteorological Satellite Studies (CIMSS), University of Wisconsin-Madison, Madison, Wisconsin, USA

³Space Science and Engineering Center (SSEC), University of Wisconsin-Madison, Madison, Wisconsin, USA

[†]Corresponding author: willem.marais@ssec.wisc.edu

March 31, 2022

Abstract

Atmospheric lidar observations provide a unique capability to directly observe the vertical column of cloud and aerosol scattering properties. However, detector and solar background noise hinder the ability of lidar systems to provide reliable backscatter and extinction (scatter) estimates. Standard methods for solving this inverse problem are only effective with high signal-to-noise ratio observations that are only available at low-resolution in uniform scenes. This paper describes a novel method for solving the inverse problem with high-resolution, lower signal-to-noise ratio observations that are effective in non-uniform scenes. Specifically, the noise associated with photon-counting lidar observations can be modeled using a Poisson distribution, and state-of-the-art tools for solving Poisson inverse problems are adapted to the atmospheric lidar problem. It is demonstrated through photon-counting HSRL (High Spectral Resolution Lidar) simulations that the proposed algorithm yield inverted backscatter and scatter cross-sections (per unit volume) with smaller MSE (Mean Squared Error) values at higher spatial resolutions, compared to the standard approach. A limited case study of real experimental data is also provided where the proposed algorithm is applied on HSRL observations and the inverted optical depths are compared against those of AERONET. In addition, three case studies on real data are also provided to juxtapose the inversion results of the new and the standard approaches.

Contents

1	Introduction	1
2	Preliminary - The unknowns & the HSRL and noise models	3
3	The standard approach in inverting the backscatter and scatter cross-sections	6
4	A new approach in inverting for the backscatter and scatter cross-sections	7
5	Experimental results	12
6	Case studies to evaluate the new approach	14
7	Conclusion and future work	19
A	Thinning a Poisson distributed matrix in creating the training and testing matrices	20
B	Proof of Theorem 1	20

1 Introduction

Atmospheric lidar systems measure the profiles of attenuated backscatter. From these the profiles of backscatter and extinction cross-sections are inferred, and are used in radiative transfer models of climate models [1]. Examples of lidar systems are the NASA-CNES CALIPSO (Cloud-Aerosol Lidar and Infrared Pathfinder Satellite Observations) mission, the NASA Langley HSRL (High Spectral Resolution Lidar) instrument, the NASA CPL (Cloud Physics Lidar) instrument, the MPL (Micro-Pulsed Lidar) network and the upcoming ESA-JAXA AT Lidar (ATmospheric Lidar) which

will be on the Earthcare satellite [1, 2, 3, 4, 5]. Another example of ground-based lidar is the Wisconsin-Madison HSRL system, which is the first system for which we have developed scatter inference tools, with the intention to extend it to other lidar instruments in the near future. All these lidar systems provide the earth science community with the unique capability to resolve the atmospheric vertical structure with very high sensitivity.

For the most part the lidar signal of interest is typically weak when observing tenuous aerosols and clouds. The implication is that the photon detectors employed are typically photon starved, and the detectors produce noisy energy rate measurements ac-

accompanied with spurious detections due to the dark current [6]. Furthermore, the solar background is another noise source and it further increases the difficulty to detect small changes in the signal. An extra complication is that the lidar detector noise is in most cases non-Gaussian, and the noise variance is signal dependent [6, 7]. Thus, statistical estimators well known in the atmospheric science community, such as the “optimal estimator” or Tikhonov regularization¹ [8, 9], cannot be directly applied unless a substantial amount of averaging is employed so to invoke the central limit theorem with a strong set of assumptions.

The predominant methodology used by lidar experts to estimate the cross-sections is to 1) divide the noisy images into non-overlapping blocks, 2) average the noisy observations in each block to reduce the noise variance, 3) solve for the unknowns using a physical model for each averaged block and 4) employ a lowpass filter across the range and temporal axes after the calculations to suppress residual noise [10, 11, 12, 13]. The size of each block is not always fixed, it depends on the lidar expert’s own judgement on how much averaging should be done. Averaging can introduce unnecessary biases, since most lidar observations of clouds and aerosols are not spatially uniform. Lowpass filtering can sometimes yield satisfactory results, but it is not suited for features that have high frequency components, such as clouds that have sharp boundaries. Furthermore, current parameter inversion techniques are ill-equipped to reliably invert the desired physical parameters. For example, in single channel lidar systems such as CALIOP a type of fixed point iteration algorithm is used which is not always numerically stable [12, § 2.3.2.3].

1.1 Contributions

The primary contribution of this paper is the introduction of statistical estimators that use the noise physical model in conjunction with a lidar physical model, to fit the estimates of the backscatter and scatter cross-sections onto the noisy observations. The estimates are constrained to be spatially piecewise smooth. With this approach 1) spatial information of the noisy observations is utilized and 2) the discontinuities and high frequency components of the backscatter and scatter cross-sections are preserved. The algorithms presented in this paper are based on sound theory that guarantees uniqueness of an estimate under reasonable conditions. We demonstrate that an immediate benefit of the new algorithms, is that fewer observations have to be accumulated to increase the SNR (Signal to Noise Ratio), in order to obtain accurate estimates of the backscatter and scatter cross-sections.

We specifically focus on inverting the particulate backscatter and scatter cross-sections from low SNR photon-counting HSRL observations. The noise of photon-counting systems can be accurately modeled by a Poisson distribution [6]. Our intention is to extend our research to single channel lidar system, and other photon detection systems in the near future, such as analog mode PMT lidar systems, where the noise is Compounded Poisson [7].

The statistical estimator that we employ is known as the TV (Total Variation) PMLE (Penalized Maximum Likelihood Estimator). Compelling results have been obtained with the TV-PMLE in medical imaging systems [14, 15]. Some medical imaging systems, such as PET (Positron Emission Tomography), low-dose CT (Computed Tomography) and confocal microscopy, also use photon-counting detectors and have the same noise characteristics as photon-counting lidar system [16]. We demonstrate, through simulated observations and four case studies on real data, that the

backscatter and scatter cross-sections can be inverted at a lower SNR with smaller MSE (Mean Squared Error) and normalized MSE values compared to the standard inversion approach. We achieve this by using the algorithm SPIRAL (Sparse Poisson Image Reconstruction ALgorithm), and an adaptation of the algorithm log-SPIRAL [14, 15]. These algorithms are well established and are numerically stable under reasonable assumptions, such as the convexity of the optimization problems.

Our secondary contribution is a novel approach to estimating the lidar ratio² directly, compared to customary approach of estimating the scatter cross-sections directly. The approach we propose has the benefit of exploiting the inverted backscatter cross-sections to constrain the estimating of the lidar ratio, and hence the scatter cross-sections.

Although we mainly focus on ground based HSRL photon-counting systems, we believe that the research we present is a necessary step to further improve upon the backscatter and scatter inversion techniques for all types of single channel lidar systems, such as the space-based analog lidar systems CALIOP. In particular, it is necessary to consider the noise model if further improvements are to be made on backscatter and scatter inversion techniques. This is apposed to either assuming that the noise is Gaussian, or to not take the noise model in account at all.

1.2 Paper outline

The paper starts off in §2 with an introduction to the physical observation model and its connection to the unknown backscatter and scattering cross-sections of interest. Included in this section are the assumptions related to the physical models. Next in §3 we describe the standard approach to estimating the unknown coefficients and other contributions that had been made in inferring the unknown parameters. Our proposed approach is presented in §4. This section includes brief overviews of the PMLE and the TV seminorm. In §5 we present two simulation results to compare the performances of the standard and new approaches against each other. Thereafter in §6 we present four case studies to demonstrate the capabilities of the proposed approach. The paper ends with the conclusion and discussion of future work in §7.

1.3 Assumptions and naming convention

When we refer to the backscatter cross-section, we specifically refer to the backscatter cross-section per unit volume. The same applies to the extinction cross-section. The backscatter (extinction) cross-section is also known as the backscatter (extinction) volume coefficient in the realm of atmospheric science [12, 17]. Throughout this paper we assume that there is negligible absorption, by any atmospheric particulates, at the laser pulse wavelength. Therefore, the extinction cross-section is assumed to be equal to the scatter cross-section in this paper. Thus, we use the term scatter cross-section throughout the paper.

We primarily focus on the backscatter cross-section estimated from the parallel polarized photon-counts. It is assumed that an estimate of the depolarization coefficients are available, which are used to normalize the backscatter cross-section when estimating for the scatter cross-section.

1.4 Notation convention

The set of non-negative real numbers is denoted by \mathbb{R}_+ , and the set of non-negative integers is denoted by \mathbb{Z}_+ . To save space, we

¹Tikhonov regularization is also known as ridge regression.

²The lidar ratio is also known as the extinction-to-backscatter ratio [12, § 2.3.1.1].

squeeze a double summation term $\sum_{n=1}^N \sum_{k=1}^K$ into one $\sum_{n=1, k=1}^{N, K}$. The vector $e_n \in \mathbb{R}^N$ is a canonical vector. The symbol $\mathbf{1}_N \in \mathbb{R}^N$ represents a vector of N ones.

In several of the models described in this paper, it is more convenient to use pointwise multiplication operations than linear algebra multiplication operations. The symbol \cdot indicates that two matrices are multiplied pointwise. For example, if $A, B \in \mathbb{R}^{N \times K}$, we have that

$$e_n^T[A \cdot B]e_k = [e_n^T A e_k][e_n^T B e_k], \quad (1)$$

where with a slight abuse of notation the e_n and e_k vectors are of different lengths.

We denote the particulate backscatter and scatter cross-sections by the symbols $\nu \in \mathbb{R}_+^{N \times K}$ and $\beta \in \mathbb{R}_+^{N \times K}$; these are the primary unknown parameters of interest which are introduced in §2. Whenever ν is estimated with say algorithm number one, its estimate will be denoted by $\hat{\nu}^{alg-1}$; the same applies to β .

The matrix $Q \in \mathbb{R}^{N \times N}$ is a lower triangular matrix of ones, scaled by a constant Δr . The constant Δr is the range sampling resolution of the lidar instrument. Each row of Q represent the Riemann integral:

$$e_n^T[Q\beta]e_k = \Delta r \sum_{l=1}^n e_l^T \beta e_k. \quad (2)$$

Hence, when Q acts on a matrix β , the output is the scaled cumulative sum of each column of β .

The Poisson noisy observations of the HSRL molecular and combined channels (defined in §2.4) are denoted by $Y_m \in \mathbb{Z}_+^{N \times K}$ and $Y_c \in \mathbb{Z}_+^{N \times K}$. The letter m is an abbreviation of the word molecular, and c is an abbreviation of the word combined. The symbol $\iota \in \{c, m\}$ is used to index c and m . The mean energy rates of the Poisson noisy observations are denoted by $E[Y_\iota] = S_\iota$, and each entry in Y_ι is statistically independent from each other.

2 Preliminary - The unknowns & the HSRL and noise models

A lidar image consists of N range bins (row axis) and K profiles (column axis); a profile refers to a single column. The range and profiles are expressed in meters and seconds. The unknown parameters that we consider in this paper are the particulate scatter $\beta \in \mathbb{R}_+^{N \times K}$ and backscatter $\nu \in \mathbb{R}_+^{N \times K}$ cross-sections. The units of both these coefficients are m^{-1} . We only refer to depolarization measurements when necessary, and it is assumed that we already have an estimate of the depolarization measurements. The scatter cross-section describes the attenuation of the laser pulse due to scattering, and are always non-negative if multiple scattering is excluded from the scatter cross-section. The energy that is scattered back towards the lidar instrument is described by the backscatter cross-section. The relation between the backscatter and scatter cross-sections are described in §2.2.

In addition to the unknowns β and ν , we are also interested in what are known as the optical depth and the lidar ratio. The optical depth is the integration of the scatter cross-section between two ranges. It is denoted by the symbol $\tau \in \mathbb{R}_+^{N \times K}$ and its relation to β is $\tau \equiv Q\beta$, where $Q \in \mathbb{R}^{N \times N}$ represents integration (see §1.4). The lidar ratio is the ratio between the scatter and backscatter cross-sections and is denoted by $\mu \equiv \beta/\nu$. The reciprocal of μ represents the fraction of the total scattering observed by the lidar instrument, and is referred to as the backscatter phase function.

In the following section we give visual examples of the unknowns. To ease the introduction to the HSRL (High Spectral Resolution Lidar) system, we first describe the single scatter lidar equation. It models the relation between what a lidar instrument measures and the unknowns β and ν . With single channel lidar systems, the inversion amounts to having more unknowns than observations. In contrast an HSRL system measures can measure the scatter cross-section almost independently from the backscatter cross-section, by taking advantage of molecular doppler broadening [10, 2]. Hence, in an ideal case when there is no noise, the unknowns can be uniquely solved for with the observations of an HSRL system. We end the section by stating the assumptions we make throughout the paper in regards with the lidar models.

2.1 Visual examples of the unknown parameters

Figure 1 shows an example image of inverted particulate backscatter β using the standard approach algorithm (see §3); the lidar observations are from the Wisconsin-Madison ground based HSRL instrument [10, 18] (see §2.4). This purpose of Figure 1 is to show the non-uniformity of a typical scene. The HSRL instrument is stationary, therefore we see the backscatter of the atmosphere as it moves across the instrument. The backscatter image was averaged

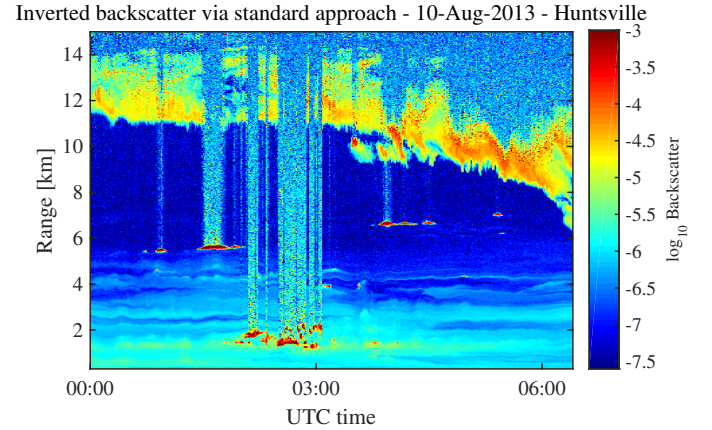


Figure 1: An example of the inverted particulate backscatter cross-section of the Wisconsin-Madison HSRL system [10, 18]. A significant amount of averaging was done to increase the SNR, which has the detrimental effect of introducing biases due to the non-uniformity of clouds and aerosols. Each hour consists of 770 columns and each 1 km range consists of about 133 rows. The vertical noisy stripes are due to the complete attenuation of the laser pulse by the clouds.

from a resolution of 7.5m (row-axis) by 2.5s (column-axis) to 30m by 30s, thus the detector noise is not clearly visible. Between 0km and 3km at 3:00 various small dense clouds are present, which have backscatter cross-section of about 10^{-3} or larger. To the left and right of these low level clouds are faint aerosol layers which have backscatter cross-section ranging from 10^{-5} to 10^{-6} . Various ripples are present on top of the aerosol layers and various “holes” or “empty” horizontal layers are present below 4km. Above 8km a large cloud is present that has backscatter cross-section that ranges from 10^{-6} to 10^{-3} .

Figure 2 show examples of the inverted backscatter and scatter cross-sections of a single profile, using the standard approach algorithm (see §3). The lidar observations were averaged over 1min. The inverted scatter cross-sections are much smoother than

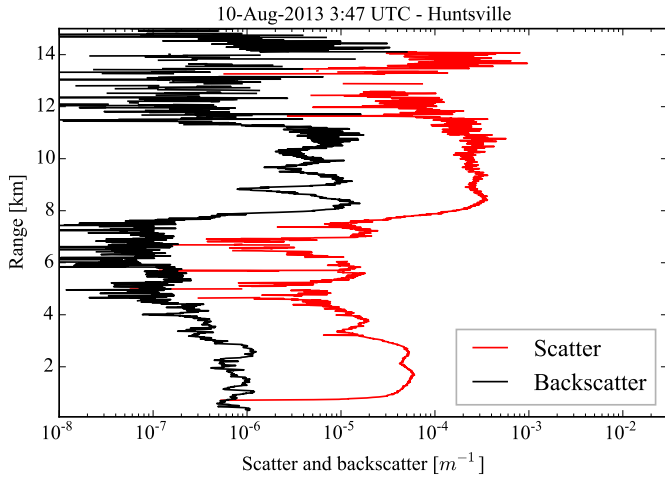


Figure 2: The black graph shows the inverted backscatter cross-section of the 1min averaged HSRL observations, corresponding to figure 1, using the standard approach algorithm (see §3). The red graph shows the corresponding inverted scatter cross-section.

the backscatter cross-sections, since the noise suppression of the standard approach was set to be very aggressive. Figure 2 gives a rough idea of how the backscatter and scatter cross-sections are related. The scatter cross-sections can be about two orders of magnitude larger than the backscatter cross-sections, and it more or less have the same upward and downward trends compared to the backscatter cross-sections.

2.2 The relation between the backscatter ν and scatter β cross-sections

In theory the backscatter phase function, the ratio between ν and β , is non-negative and has no upper bound. For example orientated platelet ice-crystals have this specific property, if a lidar instrument's laser and receiving axes are aligned with the nadir axis [19]. Most lidar systems' laser and receiving axes are at an off-nadir angle, such as CALIP and the UW-Madison HSRL [10, 20]. Hence, it can be argued that only in exceptional scenarios would the backscatter phase function exceed the value of one. Thus, throughout the rest of this paper we assume that that the backscatter cross-section is always less or equal to the scatter cross-section.

2.3 The single scatter lidar equation

To ease the introduction to the HSRL system, a brief intuitive overview of the so called single scatter lidar equation is given in this section for single polarization. The single scatter lidar equation is based on several assumption, of which the following two are the most important: 1) multiple scattering is negligible and 2) at any range r the atmosphere in the FOV is plane-parallel [17, 21]. For a detailed derivation of the single scatter lidar equation, the reader should refer to [22] or [23]. Throughout this subsection the continuous function versions of β and ν are used, and these are denoted by $\tilde{\beta}_p(r)$ and $\tilde{\nu}_p(r)$. The underscript p and index r are explained in the next paragraph.

When a visible wavelength laser pulse traverses the atmosphere, its intensity is attenuated by both molecules and particulates. Scattering, the redirection of energy, is the primary contributor to the attenuation when there is negligible absorption at the

wavelength of interest. Nitrogen gas (N_2) and oxygen (O_2) are examples of molecules that scatter radiation at visible wavelengths. Examples of particulates are smoke and ice particles. Let r [m] denote the distance between the point at which the laser pulse is currently and the lidar instrument. Let $\tilde{\beta}(r) = \tilde{\beta}_p(r) + \tilde{\beta}_m(r)$ represent the scatter cross-sections of both particulates and molecules at range r . The attenuation of the laser pulse is denoted by the transmittance $\exp(-\int_0^r \tilde{\beta}(z) dz)$; this follows from the Beer-Bouguer-Lambert's law [17]. The subscripts p and m are abbreviations of the words particulate and molecular.

At range r the energy that is scattered back towards to the lidar instrument is directly proportional to $\tilde{\nu}(r) \exp(-\int_0^r \tilde{\beta}(z) dz)$, where $\tilde{\nu}(r) = \tilde{\nu}_p(r) + \tilde{\nu}_m(r)$ is the particulate and molecular backscatter cross-section. As the backscattered energy traverses back towards the lidar instrument, it is attenuated again by a factor of $\exp(-\int_0^r \tilde{\beta}(z) dz)$. The mean energy rate measured by a lidar instrument is modeled by

$$\tilde{S}(r) = \tilde{x}(r)\tilde{\nu}(r) \exp\left(-2\int_0^r \tilde{\beta}(z) dz\right) + b, \quad (3)$$

where b is the background energy rate which includes both the dark current of the detector and the solar background radiation. Since the energy of the laser pulse is attenuated twice by $\exp(-\int_0^r \tilde{\beta}(z) dz)$, the factor 2 is present in (3). The molecular backscatter and scatter cross-sections can be precomputed using a temperature and pressure profile of the atmosphere [10].

The function $\tilde{x}(r)$ includes various calibration terms and is approximated by

$$\tilde{x}(r) = \frac{E_0 A_D c_l}{2r^2} \eta \zeta(r), \quad (4)$$

where E_0 [J] is the transmitted laser energy, A_D is the area of the telescope, A_D/r^2 is the solid angle, c_l is the speed of light and $\eta \in [0, 1]$ is the system optical efficiency. The function $\zeta(r)$ encompasses two non-ideal optical properties, since the laser pulse is not a perfect impulse. The first is the distribution of the laser energy over the target plane. The second is known as the geometric overlap function. The geometric overlap function describes the FOV (Field Of View) mismatch with the laser pulse. We assume throughout this paper that all the calibration parameters have already being estimated.

2.3.1 Discretizing single scatter lidar equation

Let N denote the total number of range bins (sampling points), uniformly spaced, for one laser shot. Each range bin n corresponds to a range $r_n \in [0, R]$ and the sampling time interval between each range bin is Δt_s . Let K denote the total number of columns. The time interval between consecutive laser shots is considered constant and is larger than $N\Delta t_s$.

The matrices $\beta \in \mathbb{R}_+^{N \times K}$ and $\nu \in \mathbb{R}_+^{N \times K}$ represent the particulate scatter $\tilde{\beta}_p(r)$ and backscatter $\tilde{\nu}_p(r)$ cross-sections (see §2.3). The matrices $\beta_m \in \mathbb{R}_+^{N \times K}$ and $\nu_m \in \mathbb{R}_+^{N \times K}$ represent the molecular scatter and backscatter cross-sections. The discretized version of (3) is defined as

$$S = x \cdot (\nu + \nu_m) \cdot \exp(-2\tau) + b \quad (5)$$

$$\tau = Q(\beta + \beta_m) \quad (6)$$

$$S, x, \tau \in \mathbb{R}_+^{N \times K}, \quad (7)$$

where Q is an integrator matrix (see §1.4). The integration is done across each column. The symbol \cdot represent the pointwise

multiplication between two matrices. The integration of the scatter cross-sections, τ , is called the optical depth.

The element $S(n, k)$ is the mean energy that the instrument measures, originating from range bin n and column k . The relation between $S(n, k)$ and (3) is

$$S(n, \cdot) = \int_{\Delta t_s} \tilde{S}(r) dt \approx \int_{\Delta t_s} \tilde{S}(r_n) dt = \Delta t_s \tilde{S}(r_n). \quad (8)$$

2.4 The HSRL physical models

Scattering due to molecules can be observed separately from scattering due to particulates, and this is what an HSRL instrument does [10, 24]. Molecules are in constant motion and their velocities are stochastic. The instrument is stationary, hence the wavelength at which the molecules scatter the photons toward the observer is Doppler-shifted [17, p. 262]. In effect the molecules broadens the frequency spectrum of the single frequency laser pulse as a function of atmosphere temperature, and this is referred to as Doppler broadening. In the context of this paper, doppler broadening due to aerosol particles is negligible compared to molecular Doppler broadening.

A typical HSRL system has two channels, which we will refer to as the combined and molecular channels. With these two channels the inversion of the backscatter ν and scatter β are more constrained than a single channel lidar system. Prior to the two channels, just before they are split into separate channels, the solar background energy rate is reduced by a bandpass filter [2, 24]. A band reject filter, such as an iodine filter, can be used to suppress the particulate contribution in the single scatter lidar equation; refer to Figure 1 in [2] for an illustration of this. The corresponding physical model for the molecular channel, after the band rejection, is

$$S_m = x_m \cdot (\nu \cdot \theta_m + \nu_m \cdot \phi_m) \cdot \exp(-2\tau) + b_m. \quad (9)$$

The calibration term $\theta_m \in [0, 1]$ represents the attenuation due to solar bandpass and the molecular band-reject filters. The calibration term $\phi_m \in [0, 1]^{N \times K}$ represents the fraction of the molecular broadened signal that is not filtered by the solar bandpass and band-reject filters. And b_m represent the solar background energy rate with the dark current energy rate for the molecular channel. The coefficients x_m also include the system optical inefficiencies for the molecular channel.

The second channel - the combined channel, corresponds to the signal just after the solar bandpass filter. The corresponding physical model for the combined channel is

$$S_c = x_c \cdot (\nu \cdot \theta_c + \nu_m \cdot \phi_c) \cdot \exp(-2\tau) + b_c, \quad (10)$$

The calibration term $\theta_c \in [0, 1]$ represents the attenuation due to solar bandpass filter; it is larger than θ_m . The calibration term $\phi_c \in [0, 1]^{N \times K}$ represents the fraction of the molecular broadened signal after the solar bandpass filter. The coefficients x_c , like the x_m , include the system optical inefficiencies that is specific to the combined channel.

Figure 3 shows an example of noisy observations of S_m and S_c , where $Y_i \sim \text{Poisson}(S_i)$. These noisy observations are of a single column of the observations that were used to create Figures 1 and 2. Observe that Y_m is smoother than Y_c , since the molecular channel primarily measures the attenuated backscatter of molecules, whereas the combined channel is very sensitive to particulate backscatter. This is due to $\theta_m \ll \theta_c$. Also notice also that rate at which the photon counts decrease, which is due to the acceptance solid angle A_D/r^2 and the attenuation of the laser pulse.

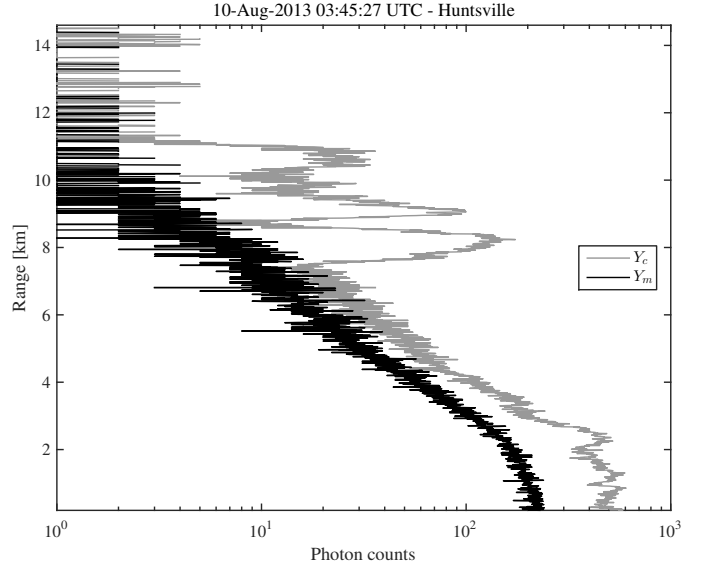


Figure 3: An example of noisy observations of molecular S_m and combined S_c channels, where $Y_i \sim \text{Poisson}(S_i)$. These noisy observations are of a single column of the observations that were used to create figures 1 and 2. The range resolution is 7.5m and the temporal resolution of the profile is 2.5s.

2.5 The physical noise model

It is well-known that the noise of a photon-counting system can be modeled by a Poisson PMF (Probability Mass Function) [6, 16]. Let $Y_i \in \mathbb{Z}_+^{N \times K}$ be the Poisson noisy observations of S_i , where $i \in \{c, m\}$. The Poisson PMF of Y_i is defined as

$$\mathbb{P}(Y_i = y) = \prod_{n=1}^N \prod_{k=1}^K \exp(-S_{i,n,k}) \frac{(S_{i,n,k})^{y_{n,k}}}{y_{n,k}!} \quad (11)$$

$$S_{i,n,k} = e_n^T \mathbb{E}[Y_i] e_k \quad (12)$$

$$y_{n,k} = e_n^T(y) e_k, \quad (13)$$

where e_n and e_k are canonical vectors and with a slight abuse of notation these two vector differ in lengths (see §1.4). The PMLE (Penalized Maximum Likelihood Estimator) is a well-known technique which uses the noise model to fit the desired parameters to the noisy observations, where the desired parameters are constrained to enforce some a priori information [25, 16, 26]. We show in §4 how the HSRL physical models are use in conjunction with the Poisson noise model to infer the scatter β and backscatter ν cross-sections.

2.6 Further assumptions about HSRL models

The HSRL instrument data that are used in this paper is from the Wisconsin-Madison HSRL [18, 10]. The telescope and detector configuration is mono-axial and avalanche Geiger-mode photodiodes are used as photon detectors [27]. The vertical spatial resolution is 7.5m and the horizontal temporal resolution is 2.5s. The wavelength of the laser pulse is 532nm. Refer to [10] for a complete description of the Wisconsin-Madison HSRL system.

There are several non-ideal system characteristics that we don't take in account in this paper. These non-ideal characteristics are non-trivial to solve; we list these for the sake of clarity.

2.6.1 Multiple scattering

The heuristic derivation of the single scatter lidar equation in §2.3 assumes that the scattered laser energy, is either scattered 1) directly towards the receiver or 2) outside of the lidar receiver field of view. This is problematic if the ratio between the radius of the particulates and the laser wavelength is approximately greater than $1/2\pi$. According to Mie theory, the forward diffraction increases as the radius of the particulates increases. Thus, the assumption of the single scatter lidar equation does not hold in such cases and multiple scattering becomes more apparent. Decreasing the FOV angle decreases the incoming energy rate due to multiple scattering [28].

2.6.2 Detector saturation

An avalanche Geiger-mode photodiode saturates when it is exposed to significant energy rates, and the saturation effect is non-linear [27]. This occurs when the incoming photon rate exceeds the linear regime of the detector. We only account for saturation due to the transmitted laser pulse, and assume that the saturation due to clouds is insignificant. Refer to [27] for more details in regards about the non-linear saturation effects of avalanche Geiger-mode photodiodes.

3 The standard approach in inverting the backscatter and scatter cross-sections

Ideally when there is no detector noise and the calibration parameters are fully known, the unknowns ν and β can be solved algebraically. We have

$$\nu = \nu_m \cdot \frac{(S_c - b_c) \cdot \frac{\phi_m}{x_c} - (S_m - b_m) \cdot \frac{\phi_c}{x_m}}{(S_m - b_m) \cdot \frac{\theta_c}{x_m} - (S_c - b_c) \cdot \frac{\theta_m}{x_c}} \quad (14)$$

and

$$\tau = Q\beta \quad (15)$$

$$= -\frac{1}{2} \log_e \left[\frac{(S_c - b_c) \cdot \frac{\theta_m}{x_c} - (S_m - b_m) \cdot \frac{\theta_c}{x_m}}{\nu_m \cdot (\phi_c \cdot \theta_m - \phi_m \cdot \theta_c)} \right] - Q\beta_m. \quad (16)$$

The scatter cross-section β can be obtained from τ using a discrete derivative operation.

The standard approach relies on either block or moving averaging to reduce the noise variance. With block averaging a lidar scene is divided into non-overlapping blocks, and an average is calculated for each block. With moving averaging a sliding block is used, which is equivalent to a two-dimensional convolution of the image with a normalized two-dimensional rectangular function. Typically block averaging is used, where the block averaging is done over distinct features such as clouds and clear-sky. Moving averages are typically not used, since a pure molecular signal can adversely bias the inversion of the scatter cross-section, when averaging is done at a cloud boundary.

The standard approach of inverting the particulate backscatter and scatter cross-sections from noisy observations can be summarized into three steps [10].

1. The measured energy rates Y_c and Y_m are either block averaged or a moving average is used to reduce the noise. The rectangular block size of either averaging technique is manually set by a lidar expert.

2. Next the averaged energy rates are plugged into (14) and (15) to obtain estimates of ν and $Q\beta$.
3. In order to obtain an estimate of β , the estimate of $Q\beta$ has to be differentiated. A lowpass filter is used prior to applying a discrete derivative so to prevent the aggravation of any noise. For example in [10] one lowpass filter is applied across the temporal axis, then another lowpass filter on the range axis. The passband widths of the lowpass filters are set manually.

Algorithm 1 concisely describes the necessary steps to invert for ν and β . Figure 2 shows an example of inverted backscatter and scatter cross-sections of Algorithm 1.

Algorithm 1 *The standard approach in the inverting for the backscatter ν and scatter β cross-sections. Typically the tuning parameters of F^{Avg} and F^{Low} are set by a lidar expert or an automated system. Note that whenever the unknown parameters are estimated with this algorithm, it is indicated by a superscript $\text{alg} - 1$.*

Let $F^{\text{Low}}(\cdot)$ be a lowpass filter function, and let $F^{\text{Avg}}(\cdot)$ be an averaging function. And let $F^{\text{Diff}}(\cdot)$ be a discrete derivative operator.

- 1: $S_c^{\text{Avg}} = F^{\text{Avg}}(Y_c)$
 - 2: $S_m^{\text{Avg}} = F^{\text{Avg}}(Y_m)$
 - 3: $\hat{\nu}^{\text{alg}-1} \leftarrow$ plug S_c^{Avg} and S_m^{Avg} into (14)
 - 4: $\tau^{\text{alg}-1} \leftarrow$ plug S_c^{Avg} and S_m^{Avg} into (15)
 - 5: $\hat{\beta}^{\text{alg}-1} = F^{\text{Diff}}(F^{\text{Low}}(\tau^{\text{alg}-1} - Q\beta_m))$
 - 6: $\hat{\mu}^{\text{alg}-1} = \hat{\beta}^{\text{alg}-1} / \hat{\nu}^{\text{alg}-1}$
 - 7: **return** $\hat{\nu}^{\text{alg}-1}, \hat{\beta}^{\text{alg}-1}, \hat{\mu}^{\text{alg}-1}, \hat{\tau}^{\text{alg}-1}$
-

3.1 An overview of other inversion methods

Past research, similar to ours, has investigated inference of the particulate backscatter ν and scatter β cross-sections. Our contribution relies on a HSRL system that has the benefit of not having to make a priori assumptions about the lidar ratio, whereas some of the cited contributions only use a single channel lidar system. With a single channel lidar system stronger assumptions have to be made about the relation between the scatter and backscatter cross-sections, since two unknowns have to be estimated from one set of observations. Hence, a direct comparison cannot be made between this paper's contribution and some of the contributions cited in this section. Nevertheless, we list the past contributions to highlight the advantages of the proposed method.

Averaging is the standard noise reduction method for lidar observations in combination of other noise suppressing techniques [10, 11, 12, 13]. In [10] a Savitzky-Golay lowpass filter is used to suppress residual noise prior to retrieving the particulate scatter cross-section from HSRL observations (see step 3 of Figure 1) [29]. This has the drawback of smoothing the desired signal itself and inadvertently introducing significant estimation biases to the inverted cross-sections on top of the bias introduced by averaging. The algorithm developed in [12] tries to avoid biasing due to averaging, by selectively applying different amounts of averaging on pre-classified features. In our contribution we try to do the least amount of accumulations of photon counts, and use a penalty function which does not impose over-smoothing constraints on the estimated cross-sections and introduce less bias. We demonstrate in §5 and §6 the backscatter can be inverted at a higher resolution than the standard approach.

In [30] the physical model was transformed into linear system which acts on a scatter cross-section vector. The scatter cross-section vector is solved for by employing the iterative Levenberg-Marquardt algorithm. The solution for the scatter vector is regulated by choosing the number of iterations of the algorithm, and this is achieved by using the L-curve method [30]. Although it is not explicitly stated, it seems that it is implicitly assumed in [30] that the noise is Gaussian distributed whereas in our approach we use a more accurate Poisson noise model.

A recent suggested approach relies on a transform method to remove high frequency components from the measured energy rates of a single channel lidar system [31]. The transform method, referred to as the empirical mode decomposition, decomposes the measured energy rates into low and high frequency components [31]. It appears that in [31] it is assumed that the noise can have negative values and therefore is not Poisson, even though the lidar instrument that [31] refers to employs photon-counting [32]. Again, our proposed approach uses the more accurate Poisson noise model.

4 A new approach in inverting for the backscatter and scatter cross-sections

Our goal with the new approach is to invert the scatter β and backscatter ν cross-sections at lower SNRs compared to the standard approach. In other words a smaller number of photon-counts have to be accumulated, vertically and temporally, to increase the SNR of the observations in order to invert for β and ν . We achieve this by ensuring that the estimated cross-sections adhere to several constraints. A TV (Total Variation) smoothness constraint is imposed on ν and β , which enforce the estimates to be piecewise smooth. With block averaging the cross-section being estimated is constrained to be a single value, whereas with the TV constraint how much the estimate varies is limited. With block averaging the estimate of a block is calculated independently from the rest of the blocks, whereas with the TV constraint the whole image is taken in account. As explained in §4.1, the TV constraint ensures that the estimates are piecewise constant with few discontinuities. The TV constraint imposes no restrictions on where the discontinuities are and hence allows high-resolution estimates.

Figures 1 and 2 suggest that the backscatter and scatter cross-sections can be approximated accurately with piecewise constant functions, since both these cross-sections are piecewise smooth. In addition to imposing a smoothness constraint on ν and β , we want to use the inverted backscatter cross-sections ν to constrain the inversion of the scatter cross-sections β . We motivate this approach by noting that in the presence of Poisson noise, the estimation of β is statistically ill-posed [33]. In other words, when the estimation of β is not constrained, any small changes in the observations - due to for example Poisson noise - can lead to significant changes to an estimate of β .

We achieve our goals by employing a well known technique: the PMLE (Penalized Maximum Likelihood Estimator). The basic idea of the PMLE is that we seek estimates which 1) are a good fit to the observed data as measured using the Poisson likelihood in (11) and 2) adhere to our a priori model of piecewise smoothness. This idea can be formulated as an optimization problem in which we search over all candidate cross-sections, and choose the cross-sections which minimize the sum of the negative Poisson log likelihood and a penalty term which is smaller for piecewise smooth cross-sections with small TV. The MLE use the noise model to fit the desired parameters on the noisy observations and it is

based on well established theorems [26]. The TV seminorm has been used in several other signal-processing applications to promote piecewise smoothness with satisfactory results [14, 34, 15]. A regularization parameter is used to set the degree to which the smoothness is promoted, and the regularization parameter is automatically set using a cross validation heuristic [15]. We adopt the algorithms SPIRAL and log-SPIRAL to compute the PMLE [14, 15].

In order to guarantee the uniqueness of the backscatter and scatter estimates, the single scatter lidar equation has to be reparameterized. The reparameterization and the formulation of the TV-PMLE are discussed in the subsection §4.2. The algorithm of the new approach is presented in §4.3. The conditions under which the estimate of the scatter cross-section β are unique is discussed in §4.4.

4.1 Overview of the MLE and the behaviour of the TV seminorm

This section gives a brief overview of the MLE and the TV seminorm, to aid the reader who is unfamiliar with both these concepts. The reader should refer to [8], [26] or any good statistics textbook for more detailed information of the MLE technique.

4.1.1 The MLE and PMLE techniques

Suppose we observe the output of a linear system, where the observation are contaminated with AWGN (All White Gaussian Noise) and the noise standard deviation is σ . Furthermore, suppose we want to estimate the parameters from the observations, on which the linear system acted. Denote the observations by y_1, \dots, y_N and the linear system by $A\omega$, where $\omega \in \mathbb{R}^K$ are the unknown parameters and $A \in \mathbb{R}^{N \times K}$. With this a noisy observation y_n can be modeled as

$$y_n = \sum_{k=1}^K A_{n,k}\omega_k + z_n = e_n^T A\omega + z_n, \quad (17)$$

where $z_n \sim \text{Gaussian}(0, \sigma^2)$ and the symbol $A_{n,k}$ indicates that we are selecting the n^{th} row and k^{th} column of the matrix A .

The basic idea of the MLE is to find the parameters ω , for a given set of observations y_1, \dots, y_N , that maximizes the joint PDF (Probability Density Function) of the observations. This is normally referred to maximizing the likelihood function, since with a PDF the parameters are held fixed and the realization of the random variables (e.g. the noisy observations) are variables. Maximizing the joint Gaussian likelihood function of white-Gaussian noise, is equivalent the minimizing the negative logarithm of the joint likelihood function. Hence, the parameter estimation of our example is simply written by

$$\hat{\omega} = \underset{\omega \in \mathbb{R}^K}{\operatorname{argmin}} \sum_{n=1}^N (y_n - e_n^T A\omega)^2 = \underset{\omega \in \mathbb{R}^K}{\operatorname{argmin}} \|y - A\omega\|_2^2. \quad (18)$$

If $K = 1$ such that $\omega \in \mathbb{R}$ and $A = 1$ is a scalar, then the estimator $\hat{\omega}$ is simply the average of the observations. Note that if the noise was not Gaussian and $K > 1$, the function to be minimized will be different from (18).

If the column rank of the matrix A is K , then the MSE of \hat{x} can be analytically derived:

$$\mathbb{E}[\|\omega - \hat{\omega}\|_2^2] = \sigma^2 \operatorname{tr} \left([A^T A]^{-1} \right), \quad (19)$$

where $\text{tr}(\cdot)$ is the trace operator. So we can see that MSE of $\hat{\omega}$ is approximately directly proportional to $\sigma^2 K/N$. It clear that it is preferable to have $N \gg K$.

If it is not possible to have $N \gg K$, it is required to constrain the parameters ω by incorporating some a priori information. Suppose we know a priori that the majority of the elements of ω are zero. In other words, the parameter is known to be sparse. A well known technique to constrain ω to be approximately sparse, is the constraint the absolute value norm of ω :

$$\|\omega\|_1 = \sum_{k=1}^K |\omega_k|; \quad (20)$$

refer to [8, §3.4] for more detailed information about this constraint. To incorporate the absolute value norm constraint into the optimization problem (18), we can reformulate the problem as a Lagrange optimization problem. Suppose we want $\|\omega\|_1$ to be upper bounded by say $\gamma > 0$. The Lagrange optimization problem is then

$$\hat{x}(\lambda) = \underset{x \in \mathbb{R}^K}{\text{argmin}} \|y - Ax\|_2^2 + \lambda(\|x\|_1 - \gamma), \quad (21)$$

where $\lambda \geq 0$ is the Lagrange multiplier and $\hat{\omega}(\lambda)$ shows that the estimate depends on the value of the Lagrange multiplier. If $K = N$ and A is an identity matrix, the estimate $\hat{\omega}(\lambda)$ has an analytical solution [8]. If A is not an identity matrix, various algorithms exist to obtain $\hat{\omega}(\lambda)$, for example SpaRSA (Sparse Reconstruction by Separable Approximation)[35]. The appropriate Lagrange multiplier value λ is obtained by fulfilling the KKT (Karush-Kuhn-Tucker) conditions [36].

If it is not known a priori what the upper bound of $\|\omega\|_1$ should be, then λ is chosen using an error criteria or a cross-validation technique. In this case the estimator (21), without the term $\lambda\gamma$, is known as a PMLE (Penalized MLE). And λ is called the regularizer parameter, and is also known as the tuning parameter.

4.1.2 The TV seminorm

A variant of the TV seminorm of a vector $\omega \in \mathbb{R}^N$, is the l1-norm of the discrete derivative of the vector:

$$\|\omega\|_{\text{TV}} = \sum_{n=1}^{N-1} |\omega_{n+1} - \omega_n|. \quad (22)$$

If $\|\omega\|_{\text{TV}}$ is used a constraint in conjunction with the MLE technique, the discrete derivative will be approximately sparse. This implies that the constrained estimate will be approximately piecewise constant. The amount of sparsity that is induced depends on how large the regularizer parameter λ is.

Figure 4 illustrates these concepts, where a white-Gaussian noisy signal has been denoised using the TV seminorm with two different regularizer values. It also show the discrete derivative of each denoised signal. Let $n = 1, \dots, N$. The true signal is

$$\omega_n = \begin{cases} 1 + (t_n - 0.25)^2 & t_n \in [0, 0.5) \\ 1.75 - t_n & t_n \in [0.5, 1) \end{cases}, \quad (23)$$

where $t_n = (n-1)/N$, $N = 128$ and the noisy signal is $y_n \sim \text{Gaussian}(\omega_n, 0.05)$. Each denoised signal is the minimizer of the optimization problem

$$\hat{\omega}(\lambda) = \underset{\omega \in \mathbb{R}^N}{\text{argmin}} \|y - \omega\|_2^2 + \lambda \|\omega\|_{\text{TV}}, \quad (24)$$

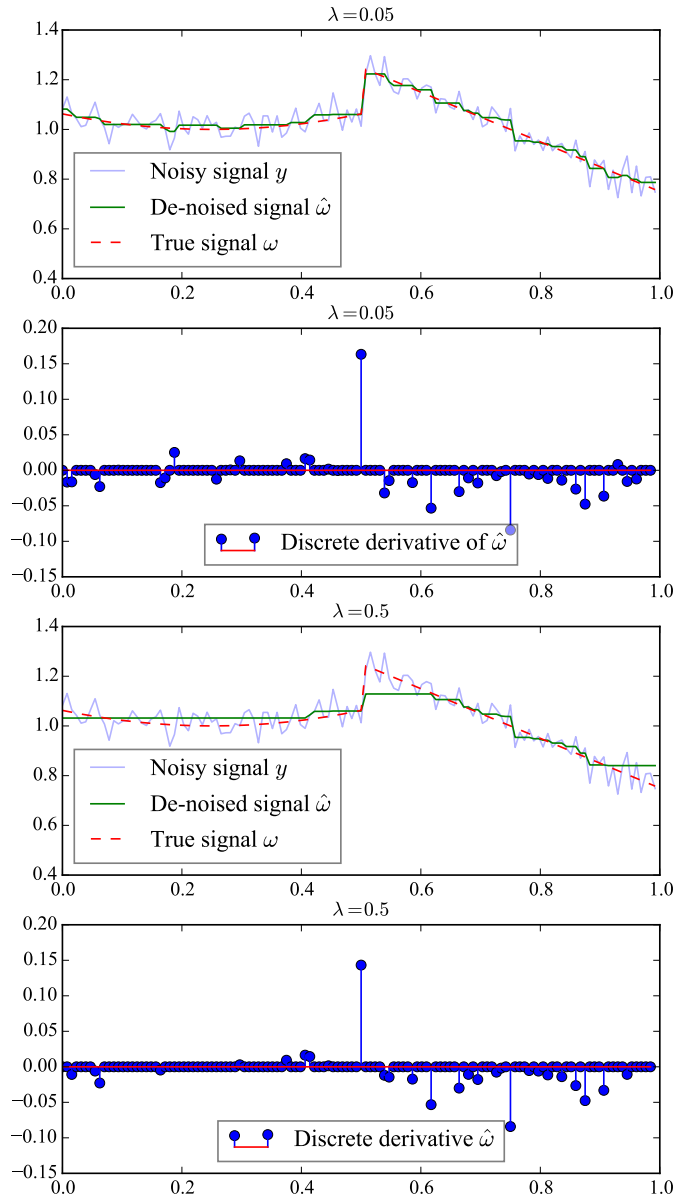


Figure 4: Examples of denoised signals using the TV seminorm. Each denoised signal is a minimizer of (24) for different regularizer values. The topmost image shows the denoised signal when $\lambda = 0.05$, and the image below it shows the sparsity of the discrete derivative of the denoised signal. The third image shows when a larger regularizer value $\lambda = 0.5$ is used, and the bottommost image shows that the sparsity of discrete derivative of the denoised signal has been increased.

where $\omega = [\omega_1, \dots, \omega_N]^T$ and $y = [y_1, \dots, y_N]^T$. The algorithm FGP of [37] has been used to obtain the denoised signals.

The topmost image shows the denoised signal for $\lambda = 0.05$, where in this case $\|\hat{\omega}(\lambda)\|_{\text{TV}} = 1.01$. The image below it shows the discrete derivative of the denoised signal. Observe that the majority of the derivative coefficients are close to being zero. The third image shows the denoised signal for a larger regularizer value $\lambda = 0.5$, where in this case $\|\hat{\omega}(\lambda)\|_{\text{TV}} = 0.42$. The variation of the denoised signal has been decreased, and its first derivative (bottommost image) is sparser compared to when $\lambda = 0.05$.

4.2 Formulation of TV-PMLE optimization problem and the algorithm

First in §4.2.1 we describe the formulation of the TV-PMLE when estimating the backscatter cross-section ν . The inverted backscatter is then used to constrain the estimation of the scatter cross-section β , which is described in the following subsection §4.2.2.

4.2.1 Inversion of the backscatter cross-section ν

To estimate the backscatter, we reparameterize the HSRL models (9) and (10). Let $f_i(\cdot)$ be the reparameterization of S_i , which is defined as

$$f_i(\omega_i) = B_i \cdot \omega_i + b_i \quad (25)$$

$$B_i = x_i \cdot \nu_m \cdot \phi_i \cdot \exp(-2Q\beta_m) \quad (26)$$

$$\omega_i = \left(\frac{\nu \cdot \theta_i}{\nu_m \cdot \phi_i} + \mathbb{1}_{N \times K} \right) \cdot \exp(-2Q\beta), \quad (27)$$

where $\omega_i \in \mathbb{R}_+^{N \times K}$ are the unknown parameters. The symbol \cdot indicates pointwise multiplication and Q is the integrator matrix (see §1.4). The matrix $\mathbb{1}_{N \times K} \in \mathbb{R}^{N \times K}$ is a matrix of ones. The quantities B_i and b_i are assumed to be known, as they can typically be estimated via system calibration. With this formulation the backscatter ν is a function of ω_i and is expressed by

$$\nu = \frac{\omega_c - \omega_m}{\omega_m \cdot a_c - \omega_c \cdot a_m}, \text{ where } a_i = \frac{\theta_i}{\nu_m \cdot \phi_i}. \quad (28)$$

The divisions are pointwise operations.

With the MLE technique the estimate $\hat{\omega}_i$ is obtained, for a given Y_i , by minimizing the negative log-likelihood of (11) with respect to the constraint $\omega_i \in \mathbb{R}_+^{N \times K}$. A penalty function is added to the MLE to regularize the estimate of ω_i . If is reasonable to assume that ω_i can be approximate with piecewise constant functions, then an adequate penalty function is the TV seminorm; a brief overview of the TV seminorm was given in §4.1. The specific TV seminorm that is used in this paper is

$$\|\omega\|_{\text{TV}} = \sum_{n=1, k=1}^{N-1, K} |\omega_{n,k} - \omega_{n+1,k}| + \sum_{n=1, k=1}^{N, K-1} |\omega_{n,k} - \omega_{n,k+1}|, \quad (29)$$

where the subscripts in this case are indices to the rows and columns of the matrix ω . This variant of the TV seminorm is known as the anisotropic TV seminorm.

The TV-PMLE is formulated by

$$\hat{\omega}_i = \underset{\omega \in \Omega_i}{\operatorname{argmin}} \{ \ell(\omega; Y_i) + \lambda \|\omega\|_{\text{TV}} \} \quad (30)$$

$$\ell(\omega; Y_i) = \mathbb{1}_N^T [f_i(\omega) - Y_i \cdot \log_e f_i(\omega)] \mathbb{1}_K, \quad (31)$$

where $\lambda \geq 0$ is referred to as the regularizer parameter. The vectors $\mathbb{1}_N \in \mathbb{R}^N$ and $\mathbb{1}_K \in \mathbb{R}^K$ are vectors of ones, and the symbol \cdot indicates that the matrices are multiplied pointwise. Throughout this paper (31) is referred to as the loss function. A cross validation heuristic is used to choose an appropriate regularizer parameter λ [14].

The minimizer $\hat{\omega}_i$ is unique if the negative log-likelihood is strictly convex, since the TV seminorm is convex. This will hold true if none of the elements of Y_i are zero. The algorithms SPIRAL and log-SPIRAL guarantee convergence to a solution if 1) the gradient of the loss function (31) is Lipschitz continuous and 2) the objective function (30) is coercive [15, §III.D]. The loss function (31) satisfies both these conditions; refer to [15] for more details.

Interpretation of ω_i

The interpretation of ω_i is as follows. Whenever there are very few particulates in a region (the dark blue parts of Figure 1), the corresponding matrix values of β and ν will be approximately 10^{-7} . Furthermore, if a weak aerosol or cloud layer is present, the values of β and ν will be close to 10^{-6} (the light blue parts of Figure 1). Thus, optical depth will increase slowly as function of range. In other words, for a fixed k the transmittance $e_n^T \exp(-2Q\beta) e_k$ will decrease slowly as n increases. Overall, the columns of ω_i will have less pronounced exponentially decaying components when considering scenes with tenuous aerosols and clouds.

Situations when an estimate of ω_i will be inaccurate and how to resolve it

If ω_m is estimated over a dense feature, such as a water cloud, it can potentially be inaccurate. This is specifically due to the transmittance term $\exp(-2Q\beta)$: A transmittance that decreases sharply over a short range interval, cannot necessarily be accurately approximated with a piecewise constant function. To resolve this issue, an alternative is to redefine (25) and set B_i equal to $\mathbb{1}^{N \times K}$. In other words, in this case, ω_i represents the mean energy rate of the channel without the background energy rate. Subsection §4.6 describes a method for deciding whether B_i should be equal to (26) or $B_i = \mathbb{1}^{N \times K}$.

4.2.2 Inversion of the scatter cross-section β

The inverted backscatter cross-section $\hat{\nu}$ (see §4.2.1) can be used to constrain the inversion of the scatter cross-section β . We do this by estimating the lidar ratio μ using the inverted backscatter, since there is a linear relation between the lidar ratio and the scatter cross-section: $\beta = \nu \cdot \mu$. Once we obtain an estimate of β , we can then algebraically compute the estimate of the optical depth τ . This is essentially the procedure described in Algorithm 2, only Algorithm 2 also includes a cross validation procedure for choosing the tuning parameters.

To estimate the lidar ratio, we reparameterize the HSRL models (9) and (10). Let $g_i(\cdot)$ be the reparameterization of S_i , which is defined as

$$g_i(\mu, \hat{\nu}) = C_i \cdot \exp(-2Q[\hat{\nu} \cdot \mu]) + b_i \quad (32)$$

$$C_i = x_i \cdot (\hat{\nu} \cdot \theta_i + \nu_m \cdot \phi_i) \cdot \exp(-2Q\beta_m), \quad (33)$$

where $\mu \in [1, \infty)^{N \times K}$. The MLE technique is used to estimate the lidar ratio by minimizing the negative log-likelihood of (11). It is reasonable to assume that lidar ratio can be approximated by piecewise constant functions. Furthermore in the atmospheric science community the lidar ratio is typically assumed to be piecewise constant. Hence, the TV seminorm is used a penalty function to regularize the estimate of μ . The TV-MPLE is formulated by

$$\hat{\mu} = \underset{\mu \in [1, \infty)^{N \times K}}{\operatorname{argmin}} \{ \ell(\mu; Y_c) + \ell(\mu; Y_m) + \lambda \|\mu\|_{\text{TV}} \} \quad (34)$$

$$\ell(\mu; Y_i) = \mathbb{1}_N^T [g_i(\mu) - Y_i \cdot \log_e g_i(\mu)] \mathbb{1}_K, \quad (35)$$

where the loss function $\ell(\cdot, \cdot)$ has been redefined and $\lambda \geq 0$ is the regularizer parameter. The loss function (35) is not necessarily strictly convex for all $\mu \in [1, \infty)^{N \times K}$, unless $b_i = 0$. Subsection §4.4 describes for what values of μ are (35) strictly convex. Also the gradient of (35) is not Lipschitz continuous, since $\exp(\cdot)$ is not a Lipschitz continuous function. Thus μ has to be constrained to a closed subset of $[1, \infty)^{N \times K}$ so that the conditions can be met under which the log-SPIRAL algorithm converge to a minimizer.

4.3 The algorithm and details regarding it

A succinct outline of the new algorithm is given in Algorithm 2. To make Algorithm 2 more readable, the details regarding TV-PMLE and the cross-validation are presented in Algorithm 2-a. The backscatter cross-section is inverted between lines 2 and 6 in Algorithm 2, and the inverted backscatter is denoted by $\hat{\nu}^{alg-2}$. Then $\hat{\nu}^{alg-2}$ is used to invert for the lidar ratio between lines 8 and 10, and the inverted lidar ratio is denoted by $\hat{\mu}^{alg-2}$. Thereafter the scatter cross-section and the optical depth are computed, and these are denoted by $\hat{\beta}^{alg-2}$ and $\hat{\tau}^{alg-2}$.

Algorithm 2 *The new approach in inverting for the particulate backscatter ν and scatter β cross-sections. Note that whenever the unknown parameters are estimated with this algorithm, it is indicated by a superscript $alg-2$.*

```

1: /* Invert the backscatter cross-section */
2: Set  $\ell(\omega; Y_i) = \mathbb{1}_N^T [f_i(\omega) - Y_i \cdot \log_e f_i(\omega)] \mathbb{1}_K$ 
3: for all  $i \in \{c, m\}$  do
4:    $\hat{\omega}_i = \text{Algorithm 2-a} [\ell(\omega; Y_i), Y_c, Y_m, \mathbb{R}^{N \times K}]$ 
5: end for
6:  $\hat{\nu}^{alg-2} = (\hat{\omega}_c - \hat{\omega}_m) / (\hat{\omega}_m \cdot a_c - \hat{\omega}_c \cdot a_m)$ 
7: /* Invert the scatter cross-section */
8: Set  $\ell(\mu; Y_i) = \mathbb{1}_N^T [g_i(\mu, \hat{\nu}^{alg-2}) - Y_i \cdot \log_e g_i(\mu, \hat{\nu}^{alg-2})] \mathbb{1}_K$ 
9:  $\ell(\mu; Y_c, Y_m) = \ell(\mu; Y_c) + \ell(\mu; Y_m)$ 
10:  $\hat{\mu}^{alg-2} = \text{Algorithm 2-a} [\ell(\mu; Y_c, Y_m), Y_c, Y_m, \mathcal{M}]$ 
11:  $\hat{\beta}^{alg-2} = \hat{\nu}^{alg-2} \cdot \hat{\mu}^{alg-2}$ 
12:  $\hat{\tau}^{alg-2} = Q \hat{\beta}^{alg-2}$ 
13: return  $\hat{\nu}^{alg-2}, \hat{\beta}^{alg-2}, \hat{\mu}^{alg-2}, \hat{\tau}^{alg-2}$ 

```

Algorithm 2-a *The TV-PMLE with cross-validation to estimate either ω_i or μ ; see Algorithm 2.*

Input: A loss function such as $\ell(\psi; Y_c, Y_m)$, the Poisson noisy matrices Y_c, Y_m and the constraint set Ψ for ψ .

```

1:  $Y_c^{trn}, Y_c^{tst} \leftarrow \text{Poisson Thinning}(Y_c)$ 
2:  $Y_m^{trn}, Y_m^{tst} \leftarrow \text{Poisson Thinning}(Y_m)$ 
3: for all  $\lambda$  in  $\Lambda$  do
4:    $\hat{\psi}(\lambda) = \underset{\psi \in \Psi}{\text{argmin}} \{ \ell(\psi; Y_c^{trn}, Y_m^{trn}) + \lambda \|\psi\|_{TV} \}$ 
5: end for
6:  $\lambda^* = \underset{\lambda \in \Lambda}{\text{argmin}} \ell(\hat{\psi}(\lambda); Y_c^{tst}, Y_m^{tst})$ 
7: return  $\hat{\psi}(\lambda^*)$ 

```

4.3.1 Backscatter inversion algorithm - lines 2 to 6

Algorithm 2-a is used to estimate $\hat{\omega}_c$ and $\hat{\omega}_m$, in order to estimate the backscatter cross-section. From lines 1 and 5, of Algorithm 2-a, a cross-validation heuristic is used to find the regularizer parameters that best constrain the estimates $\hat{\omega}_i$. The cross-validation heuristic requires two independent copies of the random matrix Y_i , and these can be created using Poisson thinning (see appendix SA) [14]. In lines 1 and 2 the Poisson noisy observations Y_i are thinned into two matrices Y_i^{trn} and Y_i^{tst} , where $Y_i = Y_i^{trn} + Y_i^{tst}$ and $\mathbb{E}[Y_i^{trn}] = 0.5 \times S_i$. The superscripts trn and tst are abbreviations of the words train and test.

Between lines 3 and 5 the unknown ω_i is estimated by varying the piecewise constant constraint with a regularizer parameter λ . The regularizer parameter λ is selected from a list of non-negative numbers Λ ; for example $\Lambda = \{10^{-2}, 10^{-1.8}, \dots, 10^{0.8}, 10\}$.

The optimization problem in line 4 is solved using the SPIRAL algorithm [15]. Since each column of B_i is strictly positive, the estimates $\hat{\omega}_i(\lambda)$ are unique when Y_i^{trn} is strictly positive.

In line 6 the regularization parameter is chosen that minimizes the loss function with Y_i^{tst} . It can be argued that the KL (Kullback-Leibler) divergence between S_i and $f(\hat{\omega}(\lambda)_i)$ is minimized in this step. Next, in line 6 of Algorithm 2 the backscatter cross-section is computed using $\hat{\omega}_c$ and $\hat{\omega}_m$; refer to (28).

4.3.2 Scatter inversion algorithm - lines 8 to 10

As with the backscatter inversion algorithm, the lidar ratios are estimated by varying a regularizer parameter λ . The set Λ will likely be different from what was used for the backscatter inversion algorithm, since lidar ratio smoothness constraint will be different.

The loss function $\ell(\mu; Y_c, Y_m)$ is not necessarily strictly convex for all $\mu \in [1, \infty)^{N \times K}$, and μ has to be constrained to a set $\mathcal{M} \subset [1, \infty)^{N \times K}$. Furthermore the set \mathcal{M} has to be bounded, since it is required that the gradient of the loss function is Lipschitz continuous. The next subsection §4.4 defines the set \mathcal{M} .

An adaptation of the log-SPIRAL algorithm is used to implement line 4 of Algorithm 2-a [14], where the gradient matrix of $\ell(\mu; Y_i)$ is

$$\nabla \ell(\mu; Y_i) = -2\hat{\nu} \cdot Q^T \left[(g_i(\mu; \hat{\nu}) - b_i) \cdot \left(\mathbb{1}_{N \times K} - \frac{Y_i}{g_i(\mu; \hat{\nu})} \right) \right]. \quad (36)$$

Once the lidar ratio is estimated, in line 10 of Algorithm 2, the scatter cross-section $\hat{\beta}^{alg-2}$ are estimated using both $\hat{\mu}^{alg-2}$ and $\hat{\nu}^{alg-2}$. Thereafter the optical depth, $\hat{\tau}^{alg-2}$, is computed by cumulatively integrating every column of $\hat{\beta}^{alg-2}$.

4.4 Ensuring uniqueness of the inverted scatter cross-section β

We will now show that Algorithm 2 can only invert scatter cross-sections that have a total optical depth less than a predefined threshold. Without loss of generality assume that $K = 1$. The Hessian matrix of the loss function $\ell(\mu; Y_i)$ (line 13 of Algorithm 2) is

$$H_i(\mu) = 4 \text{diag} \{ \hat{\nu} \} Q^T D(\mu) Q \text{diag} \{ \hat{\nu} \} \quad (37)$$

$$D(\mu) = \text{diag} \left\{ (g_i(\mu; \hat{\nu}) - b_i) \cdot \left(\mathbb{1}_N - Y_i \cdot \frac{b_i}{[g_i(\mu; \hat{\nu})]^2} \right) \right\}, \quad (38)$$

where the division is taken to be pointwise. The loss function $\ell(\mu; Y_i)$ is strictly convex if the Hessian matrix H_i is positive definite, and p.d. (positive definiteness) is ensured if

$$g_i(\mu; \hat{\nu}) > \sqrt{Y_i \cdot b_i} \quad (39)$$

$$\Rightarrow \hat{\tau} = Q[\hat{\nu} \cdot \mu] < -\frac{1}{2} \log_e \left[\frac{\sqrt{Y_i \cdot b_i} - b_i}{C_i} \right]. \quad (40)$$

In other words, there is an upper bound limit on the optical depth that can be uniquely estimated and the upper bound is influenced by the background energy rate b_i . This in turn restricts the range of scatter cross-section that can be uniquely estimated. The constraint set of μ is then

$$\mathcal{M} = \left\{ \mu \in [1, \infty)^{N \times K} : H_c(\mu) \text{ and } H_m(\mu) \text{ are p.d.} \right\}. \quad (41)$$

An easy, albeit crude, approach to determine \mathcal{M} , is to assume a single lidar ratio for the whole scene and then find the maximum lidar ratio for which the Hessian matrices are p.d. The disadvantage of this approach is that the lidar ratio upper bound can be too conservative, since clear-sky portions of a scene could have negligible lidar ratios.

4.4.1 Theoretical upper bound of the lidar ratio for given backscatter cross-section

Suppose we want to know beforehand, for given backscatter cross-section ν , whether the Algorithm 2 will be able to uniquely estimate the lidar ratio μ . We can then define the range of lidar ratio values for which the Hessian matrices of the loss functions $\ell(\mu; Y_i)$ are strictly convex with high probability. Such a situation will arise when a simulation scene is constructed to test the performance of Algorithm 2. Or when an analysis is done to determine what the range of background energy rates b_i can be tolerated in a design of an HSRL instrument, whilst ensuring that a predefined range of lidar ratios can be uniquely estimated with high probability.

We can probabilistically define the set \mathcal{M} over which the estimate $\hat{\mu}$ by Algorithm 2 is unique. We define the set \mathcal{M}_l to be such that for every $\mu \in \mathcal{M}_l$ the Hessian matrix (37) is postive definite with probability of at least ζ :

$$\mathcal{M}_l = \left\{ \mu \in [1, \infty)^{N \times K} : \mathbb{P}(H_l(\mu) \text{ is p.d.}) \geq \zeta \right\}. \quad (42)$$

Then the set \mathcal{M} is defined to be $\mathcal{M} \equiv \mathcal{M}_c \cap \mathcal{M}_m$. The following theorem provides a means with which we can define \mathcal{M} . It takes in account that Algorithm 2 does not have perfect knowledge of the backscatter cross-section ν .

Theorem 1. *Let $K = 1$ and let $\hat{S}_i = f_i(\hat{\omega}_i)$ represent the denoised Y_i , where $\mathbb{E}[Y_i] = S_i$. Suppose an oracle tells us that*

$$\frac{e_n^T \hat{S}_i}{\delta_U} \leq e_n^T S_i \leq \frac{e_n^T \hat{S}_i}{\delta_L}. \quad (43)$$

Then the lower bound on the probability that the Hessian matrix $H_l(\mu)$ is p.d. (positive definite), for a given ν and μ , is

$$\mathbb{P}(H_l(\mu) \text{ is p.d.}) \geq 1 - \sum_{n=1}^N \exp[-\zeta(n)], \quad (44)$$

where

$$\zeta(n) = e_n^T \frac{\hat{S}_i}{\delta_U} \frac{\epsilon^2(n)}{2 + 1.5\epsilon(n)} \quad (45)$$

$$\epsilon(n) = -1 + \delta_L e_n^T \left(\frac{[g_i(\mu; \hat{\nu})]^2}{b_i \cdot \hat{S}_i} \right) \quad (46)$$

with the condition that for all $n \leq N$

$$\epsilon(n) > 0 \quad (47)$$

$$\Rightarrow e_n^T g_i(\mu; \hat{\nu}) > e_n^T \sqrt{\frac{b_i \cdot \hat{S}_i}{\delta_L}} \quad (48)$$

The proof of this theorem is given in appendix §B. It should be noted that this theorem use a loose upper bound (the union bound) in the proof. Thus, the lower bound in the theorem is very conservative. A better lower bound can be derived by using the law of total probability, but with the expense of being computationally intensive. Hence, this theorem should be used with the intention to find a quick lower bound probability value.

The following list shows the steps required to use Theorem 1 to define the sets \mathcal{M}_l .

1. Set $\zeta \in (0, 0.5]$ to lower bound $\mathbb{P}(H_l(\mu) \text{ is p.d.})$ with $1 - \zeta$.
2. For a $i \in \{c, m\}$, let μ be a constant matrix. Increase the values of matrix μ until the lower bound in (44) is equal to $1 - \zeta$ and the condition (47) is satisfied. Set the maximum constant value of μ equal to u_i .
3. Define $\mathcal{M}_l = [1, u_i]^{N \times K}$.

We have now that with probability of at least $1 - 2\zeta$, the loss function in line 15 of Algorithm 2 is strictly convex on the set \mathcal{M} .

4.5 Another algorithm worthy of notice to invert the scatter cross-section β

It is not always clear whether it is better to regularize an estimate of the lidar ratio μ , and then to compute the scatter cross-section β . Or to regularize an estimate of β , and then compute the lidar ratio μ . With this in mind, Algorithm 3 shows another approach to invert the scatter cross-section β , where the reparameterized lidar model is

$$h_i(\beta, \hat{\nu}) = C_i \cdot \exp(-2Q\beta) + b_i. \quad (49)$$

The matrix C_i is defined in (33). In this case the scatter cross-section is constrained to be greater or equal to the inverted backscatter.

Algorithm 3 *Another approach in inverting for the particulate scatter cross-section β . Note that whenever the unknown parameters are estimated with this algorithm, it is indicated by a superscript $alg - 3$.*

Input: Previously inverted backscatter $\hat{\nu}$, such as $\hat{\nu}^{alg-2}$.

- 1: /* Invert the scatter cross-section */
- 2: Set $\ell(\beta; Y_i) = \mathbf{1}_N^T \left[h_i(\beta, \hat{\nu}^{alg-2}) - Y_i \cdot \log_e h_i(\beta, \hat{\nu}) \right] \mathbf{1}_K$
- 3: **for** every λ in Λ_β **do**
- 4: $\hat{\beta}(\lambda) = \underset{\beta \in \mathcal{B}}{\operatorname{argmin}} \{ \ell(\beta; Y_c^{\text{trn}}) + \ell(\beta; Y_m^{\text{trn}}) + \lambda \|\beta\|_{\text{TV}} \}$
- 5: **end for**
- 6: $\lambda^\ddagger = \underset{\lambda \in \Lambda_\beta}{\operatorname{argmin}} \ell(\hat{\beta}(\lambda); Y_c^{\text{tst}}) + \ell(\hat{\beta}(\lambda); Y_m^{\text{tst}})$
- 7: $\hat{\beta}^{alg-3} = \hat{\beta}(\lambda^\ddagger)$
- 8: $\hat{\mu}^{alg-3} = \hat{\beta}^{alg-3} / \hat{\nu}$
- 9: $\hat{\tau}^{alg-3} = Q\hat{\beta}^{alg-3}$
- 10: **return** $\hat{\beta}^{alg-3}, \hat{\mu}^{alg-3}, \hat{\tau}^{alg-3}$

As with Algorithm 2, the scatter cross-section β has to be upper bounded so that the loss function (line 4 of Algorithm 3) is strictly convex. Let \mathcal{B} be the set over which the loss function is strictly convex. The procedure given in §4.4 to define that set \mathcal{M} , can be used to define the set \mathcal{B} with some minor modifications.

4.6 How to choose the best estimate of the backscatter cross-section

As it was described in §4.2, depending on the rate of decrease of the transmittance $\exp(-2Q\beta)$, at times it is better to let B_i equal $\mathbf{1}_{N \times K}$ rather than (26). Suppose $\hat{\omega}_i^{alg-2}$ represents the inferred ω_i when B_i equals (26), and $\hat{\omega}_i^{alg-2}$ when $B_i = \mathbf{1}_{N \times K}$. We can use a log likelihood ratio test, which is part of the cross-validation heuristic, to determine whether $\hat{\omega}_i^{alg-2}$ is more accurate than $\hat{\omega}_i^{alg-2}$. Let hypothesis \mathcal{H}_0 represent the case when $\hat{\omega}_i^{alg-2}$ is more

accurate than $\hat{\omega}_i^{alg-2}$, and let \mathcal{H}_1 represent the opposite hypothesis. The log likelihood ratio test is then

$$\ell\left(\hat{\omega}_i^{alg-2}; Y_i^{tst}\right) \underset{\mathcal{H}_0}{\overset{\mathcal{H}_1}{\geq}} \ell\left(\hat{\omega}_i^{alg-2}; Y_i^{tst}\right) \quad (50)$$

$$\mathcal{H}_0: B_i = x_i \cdot \nu_m \cdot \phi_i \cdot \exp(-2Q\beta_m) \quad (51)$$

$$\mathcal{H}_1: B_i = \mathbf{1}_{N \times K}. \quad (52)$$

The function $\ell(\cdot; Y_i^{tst})$ is defined by (31) and Y_i^{tst} was described in §4.3.

5 Experimental results

Two synthetic datasets were used to juxtapose the performance of Algorithms 1, 2 and 3. The synthetic datasets were chosen to be horizontally uniform, which is beneficial for Algorithm 1. All the algorithms were expected to infer the backscatter and scatter cross-sections at a maximum range resolution. The synthetic datasets are described in §5.1. The results of the simulation experiments are presented in §5.2.

5.1 Synthetic datasets

Both the synthetic datasets represent nighttime scenes, where the background energy rate in each scene is approximately 0.5. The simulate backscatter cross-section for each scene was created by taking an actual HSRL scene,

1. average 2880 columns of the scene, which is equivalent to two hours of observations,
2. invert for the backscatter cross-section using Algorithm 1 and
3. apply a low-pass filter to suppress the residual noise.

Piecewise constant lidar ratios were used to calculate reasonable simulated scatter cross-section.

Figure 5 shows the first synthetic dataset. This dataset represents a scene with a two layer, 5km thick planetary boundary layer and clear-sky above it. The total optical depth of this scene is 0.1775. Figure 6 show the backscatter, scatter cross-sections and energy rates of the second synthetic datasets. The second synthetic dataset represent a scene with a 2km thick planetary boundary layer, with various types of cloud layers of different optical depth values. The total optical depth of the scene is 0.1496. Refer to Figure 3.3 in [28, p. 21] for a description of what each lidar ratio represents.

5.2 Simulation experiments

For the first and second simulation scenes, each column in an image represents the accumulation of several laser shots. This was done to increase the SNR of the energy rates. The temporal and spatial resolution for the two scene were $7.5m \times 30s$ and $7.5m \times 120s$, where the native row and columns resolutions are 7.5m and 2.5s. For both scenes the number of rows and columns are 1940 by 12.

For Algorithm 1 all the columns, of each scene, were averaged together. Also a SG (Savitzky-Golay) lowpass filter was used for Algorithm 1 [29], where the frame size and polynomial order differed for each simulation scene. For the first simulation scene these were set to 41 and 2. For the second simulation scene the parameters were 499 and 5. These parameters were chosen based

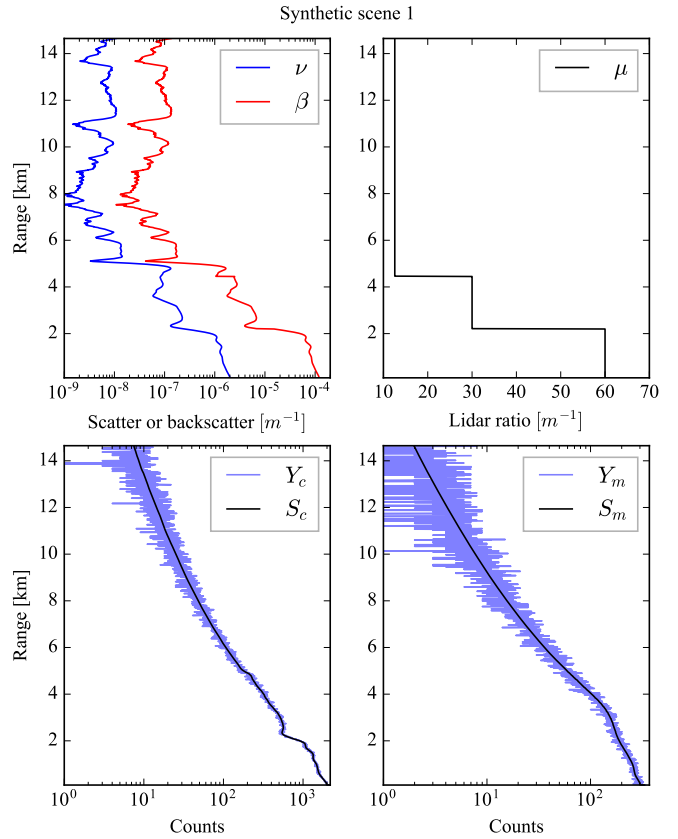


Figure 5: A column of synthetic dataset 1, which is representative of the whole scene, where no accumulation across the columns have been performed. Top left: The backscatter ν and scatter β cross-sections. Top right: The lidar ratio μ . Bottom row: An example of the energy rate observations Y_c and Y_m , with the corresponding mean energy rates S_c and S_m .

on the minimization of the MSE of the inverted scatter cross-section.

For Algorithm 2 the range of scatter cross-section that can be uniquely inverted, is limited by the background energy rate. Theorem 1 can be used to calculate an upper bound on the total maximum optical depth that can be uniquely estimated. For the first simulation scene, with probability of at least 0.999, Algorithm 2 can uniquely estimate a scatter profile that has a total optical depth of less than 0.8768. And for the second simulation scene is upper bound is 0.7643 with the same probability. Using the steps listed in §4.4, it turns out that for both simulation the maximum lidar ratio is more than a 500. Hence, we can set $\mathcal{M} = [1, 500]^{N \times K}$.

5.2.1 Error performance measurements

We consider two error measurements to compare the performance of the different algorithms. The first is the MSE (Mean Square Error),

$$\text{MSE}(\hat{\nu}^{alg-1}) = \mathbb{E} \left[\|\nu - \hat{\nu}^{alg-1}\|_F^2 \right] \quad (53)$$

$$= \underbrace{\mathbb{E} \left[\|\nu - \mathbb{E}[\hat{\nu}^{alg-1}]\|_F^2 \right]}_{\text{bias}} + \underbrace{\mathbb{E} \left[\|\hat{\nu}^{alg-1} - \mathbb{E}[\hat{\nu}^{alg-1}]\|_F^2 \right]}_{\text{standard deviation}} \quad (54)$$

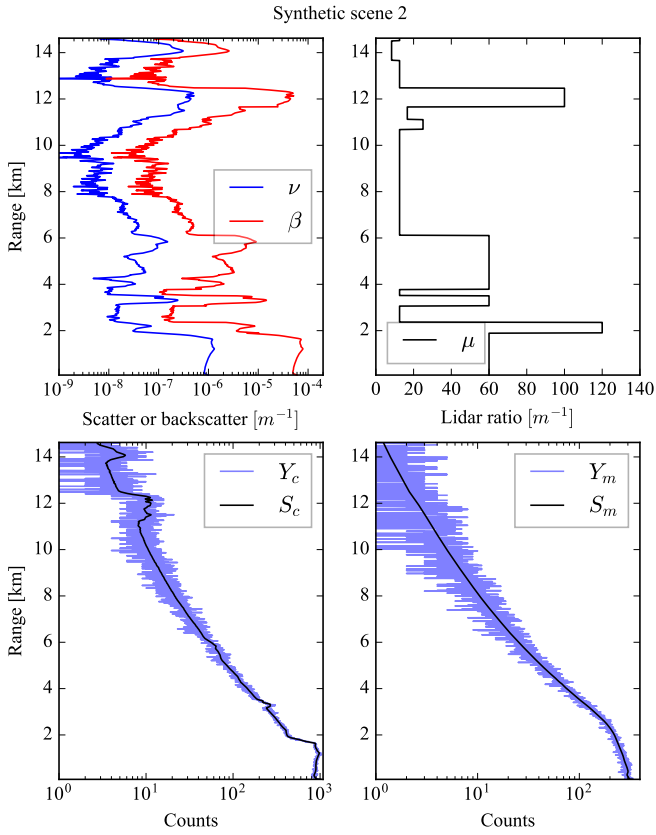


Figure 6: A column of synthetic dataset 2, which is representative of the whole scene, where no accumulation across the columns have been performed. Top left: The backscatter ν and scatter β cross-sections. Top right: The lidar ratio μ . Bottom row: An example of the energy rate observations Y_c and Y_m , with the corresponding mean energy rates S_c and S_m .

and we specifically compare the bias and standard deviation of each algorithm. The norm $\|\cdot\|_F^2$ is known as the Frobenius norm and it is defined as

$$\|\nu\|_F^2 = \text{trace}(\nu^T \nu). \quad (55)$$

The second error measurement is the R-MSE (Relative-MSE), which scales the difference between ν and $\hat{\nu}^{alg-1}$ with ν . It is defined as

$$\text{R-MSE}(\hat{\nu}^{alg-1}) = \mathbb{E} \left[\left\| \frac{\nu - \hat{\nu}^{alg-1}}{\nu} \right\|_F^2 \right]. \quad (56)$$

If an element of ν is less than one, the corresponding difference is enlarged and is therefore more significant. This error measurement is useful to compare the algorithm performance when different simulation scenes are considered.

The simulation experiments were repeated 100 times in order to obtain values for the MSE and R-MSE of the different algorithms.

5.2.2 Simulation scene 1

Table 1 shows the MSE, bias, standard deviation and R-MSE of the different algorithms. Overall in regards with MSE and R-MSE, Algorithms 2 and 3 consistently outperform Algorithm 1.

The inverted scatter and lidar ratio coefficients of Algorithm 2 have smaller error values than that of Algorithm 3, since the optimization problem of Algorithm 2 is more constrained.

The performance of Algorithm 1 can be improved by also including range averaging; for example more aggressive averaging can be done from ranges 6km to 14 km. The problem is that with Algorithm 1 a lidar expert has to manually determine the non-overlapping range-intervals over which averaging has to be done to further improve the estimate of the scatter-cross section. Furthermore, the lidar expert does not have an objective measure to determine how much averaging has to be done. In comparison Algorithms 2 and 3 circumvent these issues; Algorithms 2 and 3 impose a smoothness constraint which is automatically set using a cross-validation heuristic.

Table 1: The MSE, bias, std (standard deviation) and R-MSE measurements of the different algorithms for the first simulation. Algorithm 2 consistently outperforms the Algorithm 1. Algorithm 1 performs poorly in estimating the scatter cross-section β and the lidar ratio μ above 6km, and this is the reason for the large errors. Algorithm 2 first estimates the lidar ratio μ , then algebraically computes the scatter cross-section β and the optical depth τ , while Algorithm 3 directly estimates β and then algebraically computes μ and τ . The two approaches are comparable when it comes to estimating β and τ , but Algorithm 2 is significantly better at estimating μ .

Inversion	MSE	Bias	Std.	R-MSE
$\hat{\nu}^{alg-1}$	2.56e-16	2.42e-06	1.49e-02	1.71e+01
$\hat{\nu}^{alg-2}$	2.52e-17	5.48e-08	1.16e-03	2.74e-01
$\hat{\beta}^{alg-1}$	1.25e-08	1.27e-10	1.11e-04	4.86e+06
$\hat{\beta}^{alg-2}$	3.17e-11	5.67e-12	5.10e-06	3.45e-01
$\hat{\beta}^{alg-3}$	5.64e-11	7.78e-12	6.98e-06	1.33e+02
$\hat{\mu}^{alg-1}$	5.12e+12	5.27e+10	2.25e+06	3.24e+10
$\hat{\mu}^{alg-2}$	2.73e+01	8.35e+00	4.35e+00	3.30e-02
$\hat{\mu}^{alg-3}$	1.14e+06	1.20e+04	1.06e+03	7.19e+03
$\hat{\tau}^{alg-1}$	2.25e-04	2.42e-06	1.49e-02	1.24e-02
$\hat{\tau}^{alg-2}$	3.42e-07	2.01e-08	5.67e-04	5.48e-04
$\hat{\tau}^{alg-3}$	9.68e-07	1.75e-07	8.91e-04	5.43e-04

Figure 7 shows the inverted backscatter (first row), scatter (second row) and lidar ratio (third row) results of Algorithms 2 and 1 of one experiment. The error performance of Algorithm 2 depends on the accuracy of the inverted $\hat{\nu}^{alg-2}$. Since ν is approximated by a piecewise constant function, block-shaped artifacts can appear in the inverted $\hat{\beta}^{alg-2}$ and $\hat{\mu}^{alg-2}$; this is evident in at range 1km of the middle-right and bottom-right images of Figure 7.

5.2.3 Simulation scene 2

Table 2 shows the MSE, bias, standard deviation and R-MSE of the different algorithms applied to scene 2 data. The inverted parameters $\hat{\nu}^{alg-1}$ and $\hat{\tau}^{alg-1}$ are less biased than the other inverted parameters. But, in regards with MSE and R-MSE, Algorithms 2 and 3 outperform Algorithm 1. Algorithm 2 is the best for all parameter estimates, especially when estimating the lidar ratio μ .

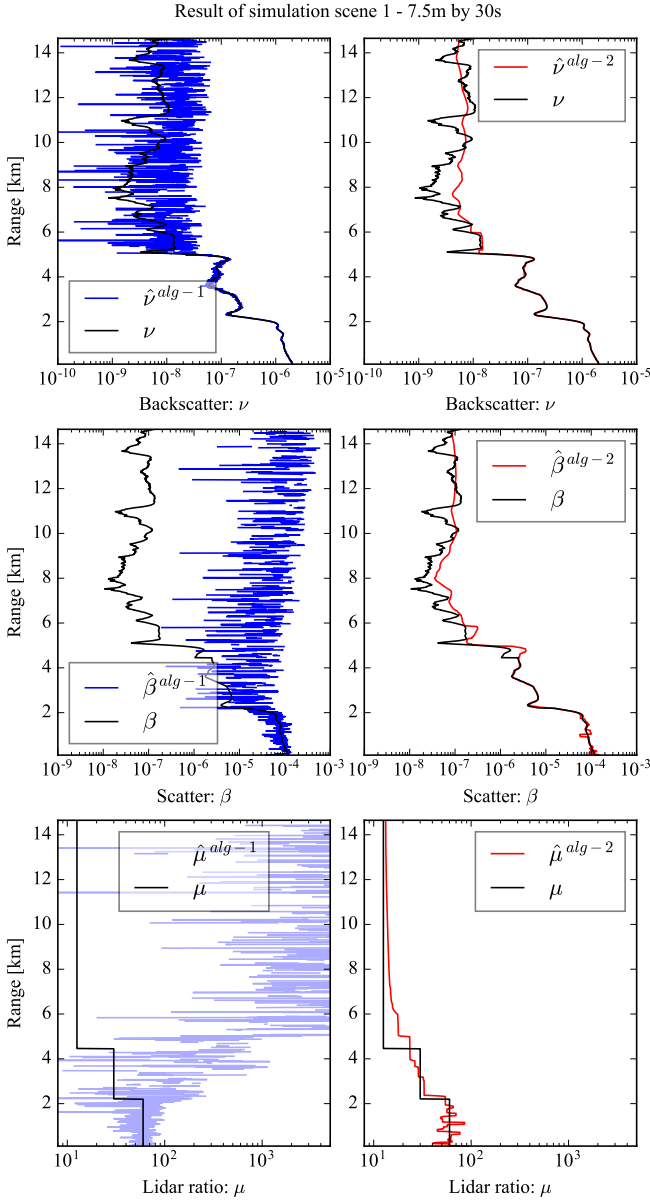


Figure 7: The six images show examples of the inverted backscatter, scatter cross-sections and lidar ratio of the first simulation scene. The black graphs in these images show the corresponding true backscatter ν , scatter β cross-sections and the true lidar ratio μ . The blue graphs in leftmost images show examples of, from top to bottom, the inverted backscatter, scatter cross-sections and lidar ratio of Algorithm 1. And the red graphs in the rightmost images show examples of the inverted cross-sections of Algorithm 2. It is clear from these images that Algorithm 2 outperforms Algorithm 1.

Figure 8 shows the inverted backscatter (first row), scatter (second row) and lidar ratio (third row) results of an experiment. In this simulation scene the SG filter's has a narrower bandpass bandwidth compared to that of the first simulation scene. Thus, Algorithm 1 can somewhat resolve the scatter cross-section between ranges 10 km and 13 km. But this is at the expense of over-smoothing the scatter cross-section below the 2 km range. Overall Algorithms 2 and 3 outperform Algorithms 1, based on

Table 2: The MSE, bias, std (standard deviation) and R-MSE measurements of the different algorithms for the second simulation. Algorithm 2 consistently outperforms Algorithms 1. Algorithm 1 performs poorly in estimating the scatter cross-section β and the lidar ratio μ between 4km and 11km, and this is the reason for the large errors. Algorithm 2 first estimates the lidar ratio μ , then algebraically computes the scatter cross-section β and the optical depth τ , while Algorithm 3 directly estimates β and then algebraically computes μ and τ . The two approaches are comparable when it comes to estimating τ , but Algorithm 2 is significantly better at estimating β and μ .

Inversion	MSE	Bias	Std.	R-MSE
$\hat{\nu}^{alg-1}$	1.49e-16	9.77e-07	9.80e-03	2.57e+00
$\hat{\nu}^{alg-2}$	1.06e-16	1.50e-06	1.02e-03	2.90e-01
$\hat{\beta}^{alg-1}$	1.08e-10	5.03e-11	7.62e-06	7.09e+03
$\hat{\beta}^{alg-2}$	1.51e-11	9.44e-12	2.37e-06	3.77e+00
$\hat{\beta}^{alg-3}$	1.76e-10	1.40e-10	5.93e-06	3.85e+03
$\hat{\mu}^{alg-1}$	5.93e+09	5.96e+07	7.66e+04	3.76e+07
$\hat{\mu}^{alg-2}$	4.34e+02	3.96e+02	6.12e+00	1.97e+00
$\hat{\mu}^{alg-3}$	1.44e+05	1.04e+05	2.01e+02	1.04e+03
$\hat{\tau}^{alg-1}$	9.70e-05	9.77e-07	9.80e-03	1.15e-02
$\hat{\tau}^{alg-2}$	3.06e-06	2.55e-06	7.13e-04	3.89e-04
$\hat{\tau}^{alg-3}$	5.42e-06	4.39e-06	1.02e-03	7.05e-04

Table 2 and Figure 8.

From the bottom right image of Figure 8 we observe that Algorithm 2 mostly overestimates the lidar ratio. Further investigation is required to determine what is necessary to further improve upon this result.

6 Case studies to evaluate the new approach

Four case studies of real experimental data are presented to juxtapose the inverted backscatter and scatter cross-sections of Algorithms 1 and 2. Each case study focuses on a specific aspect of Algorithm 2. The first case study demonstrates the capability of Algorithm 2 to invert the backscatter cross-section at a higher resolution than Algorithm 1. To validate Algorithm 2, the second case study compares the aerosol optical depth inverted by Algorithm 2 against AERONET optical depth retrievals [38]. And the last two case studies demonstrate the capability of Algorithm 2 to invert the scatter cross-section at a higher resolution than Algorithm 1.

With all four case studies, observations of the Wisconsin-Madison HSRL instrument was used, while it was situated at the DOE's SGP (Southern Great Plains) ARM (Atmospheric Radiation Measurement) site during the CHARMs³ experiment in the summer of 2015. The backscatter and scatter cross-sections were estimated from parallel-polarized photon-counts. An auxiliary cross-polarization estimate was used to normalized the backscatter cross-section estimates, when estimating for the scatter cross-section.

³Combined HSRL and Raman Measurement Study funded by the DOE.

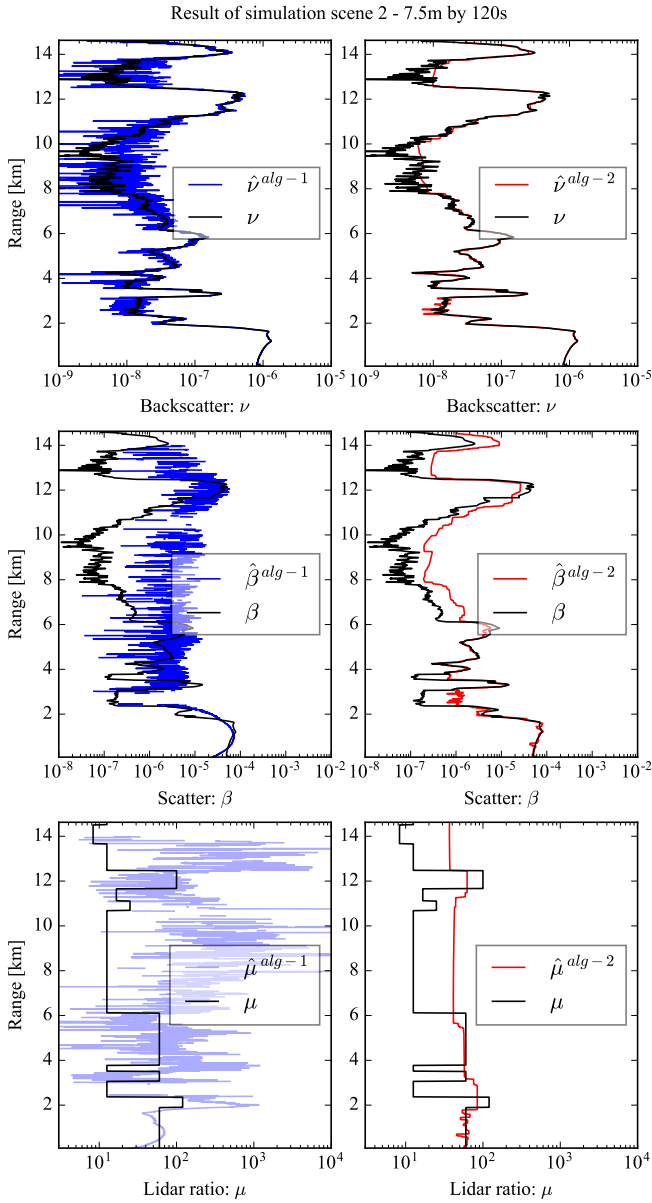


Figure 8: The six images show examples of the inverted backscatter, scatter cross-section and lidar ratio of the second simulation scene. The black graphs in these images show the corresponding true backscatter ν , scatter β cross-sections and the true lidar ratio μ . The blue graphs in leftmost images show examples of, from top to bottom, the inverted backscatter, scatter cross-section and lidar ratio of Algorithm 1. And the red graphs in the rightmost images show examples of the inverted cross-section of Algorithm 2. It is clear from these images that Algorithm 2 outperforms Algorithm 1.

6.1 Case study one - backscatter cross-section of high altitude cloud

The top image of Figure 9 shows the backscatter cross-section $\hat{\nu}^{alg-2}$ inverted with the new approach of a cirrus cloud, and the middle image shows the inverted backscatter cross-section $\hat{\nu}^{alg-1}$ of the standard approach. Both these images have a resolution of 15m by 15s. The bottommost image shows a block averaged

version of $\hat{\nu}^{alg-1}$, where the resolution is 60m by 60s. This figure demonstrates the decrease in sensitivity of noise of $\hat{\nu}^{alg-2}$ in comparison with $\hat{\nu}^{alg-1}$. Furthermore the figure also suggests that there is a gain in spatial information when using Algorithm 2, since with Algorithm 1 further averaging has to be done to reduce the residual noise.

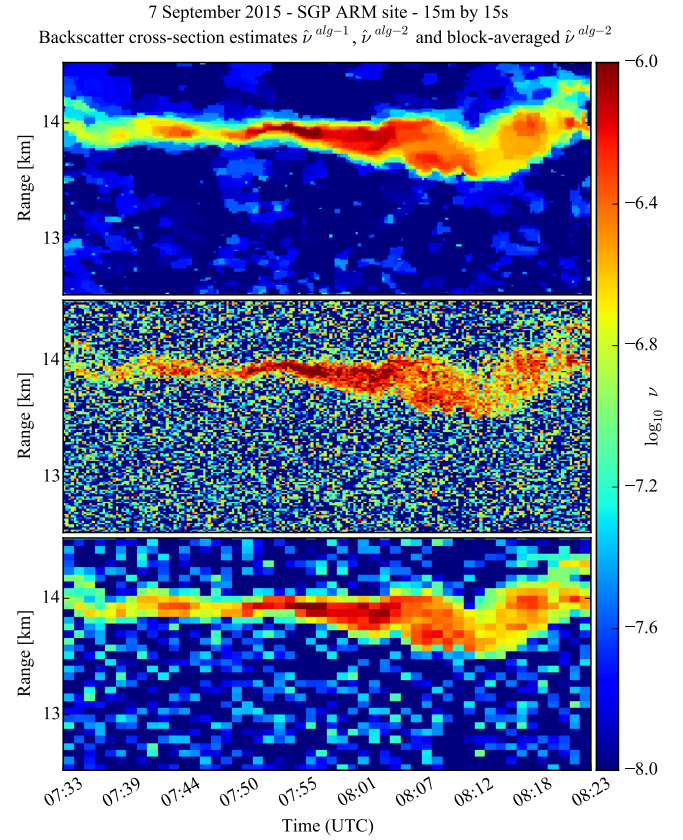


Figure 9: This figure demonstrates the gain of spatial information of the new approach (Algorithm 2). The top image shows the backscatter cross-section $\hat{\nu}^{alg-2}$ inverted with the new approach. The middle image shows the backscatter cross-section $\hat{\nu}^{alg-1}$ inverted with the standard approach (Algorithm 1). The bottommost image show a block averaged version of $\hat{\nu}^{alg-1}$, where the resolution is 60m by 60s.

Figures 10 and 11 validates the backscatter cross-section of Algorithm 2 by using a uniform aerosol scene. The resolution of the data in both figures is 7.5m by 2.5s. The leftmost image of Figure 10 shows the inverted backscatter cross-section $\hat{\nu}^{alg-2}$ of the new approach. The middle image is the inverted backscatter of the standard approach $\hat{\nu}^{alg-1}$ with no averaging. In the rightmost image another version of $\hat{\nu}^{alg-1}$ is shown where a moving average filter was used with a window-width of 1min (24 columns).

Figure 11 shows two columns of Figure 10. For the most part the inverted backscatter cross-section $\hat{\nu}^{alg-2}$ of the new approach agrees with the backscatter cross-section $\hat{\nu}^{alg-1}$ of the averaged observations. Since the scene is almost uniform, the inverted backscatter $\hat{\nu}^{alg-1}$ with moving averaging should be accurate. Furthermore, for a simple scene like we have in Figure 10, the inverted backscatter $\hat{\nu}^{alg-2}$ with the new approach should very similar compared to $\hat{\nu}^{alg-1}$; and this is confirmed by Figure 11. There are specific instances where the new approach potentially

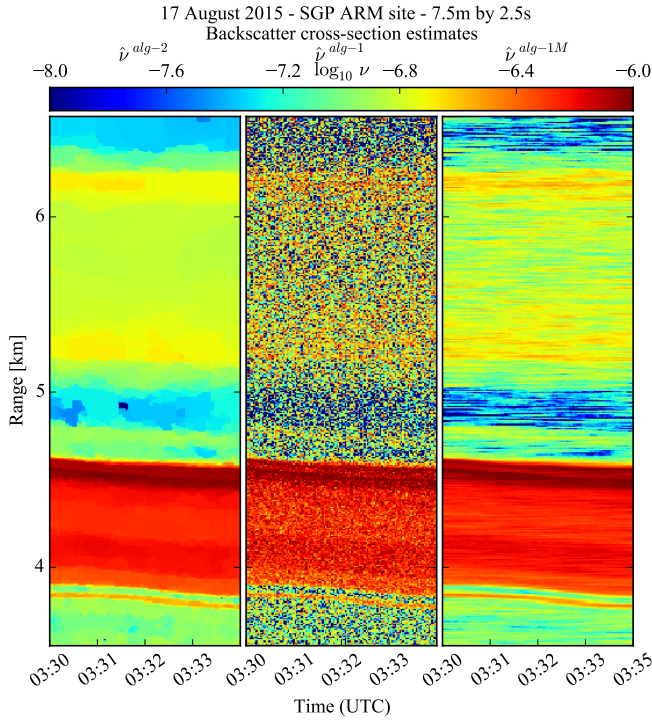


Figure 10: In conjunction with Figure 11, this figure demonstrates that the inverted backscatter cross-section of the new and standard approaches agrees with each other. The symbol $\hat{\nu}^{alg-1M}$ indicate a moving average filter was used in Algorithm 1, with a window-width of 1min (24 columns). The leftmost image is the inverted backscatter of the new approach, and the middle column is the inverted backscatter of the standard approach without averaging. The rightmost image is the inverted backscatter cross section of the standard approach, with averaging.

over-smooth the backscatter, for example at 4.6km and 6.2km.

6.2 Case study two - aerosol optical depth

To validate the inverted scatter cross-section of Algorithm 2, we compare the optical depth of it against that of AERONET. AERONET (AERosol ROBOTIC NETwork) is an instrument that measures the radiation from the sun to retrieve the aerosole optical depth [38]. Figure 12 shows the aerosole optical depth values of the new approach $\hat{\tau}^{alg-2}$, the standard approach $\hat{\tau}^{alg-1}$ and AERONET. The smallest solar zenith angle of the AERONET measurements is at 18:37 UTC.

There are several sources of uncertainty that contribute to the optical depth difference between the HSRL and the AERONET instrument. The first is the significant uncertainty in the geometric overlap function between range 0km and 5km, which is typical of all ground based lidar systems. The second uncertainty is that the HSRL instrument points away from the sun, while the AERONET line of sight is pointed towards the sun. Thus, different atmospheric columns are observed by these two instruments. Although optical depth measurements differ by between 0.06 and 0.09, the upward and downtrend in the AERONET optical depth measurements are also present in the inverted optical depth of the new approach.

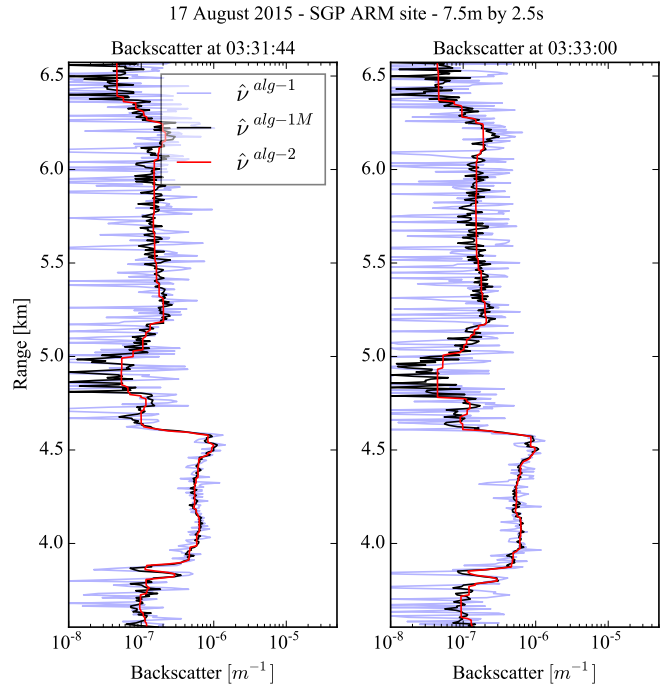


Figure 11: In conjunction with Figure 10, this figure demonstrates that inverted backscatter cross-section of the new $\hat{\nu}^{alg-2}$ and standard $\hat{\nu}^{alg-1M}$ approach agrees with each other for the most part. The symbol 1M in $\hat{\nu}^{alg-1M}$ indicates that a moving average filter was used in Algorithm 1, with a window-width of 1min (24 columns).

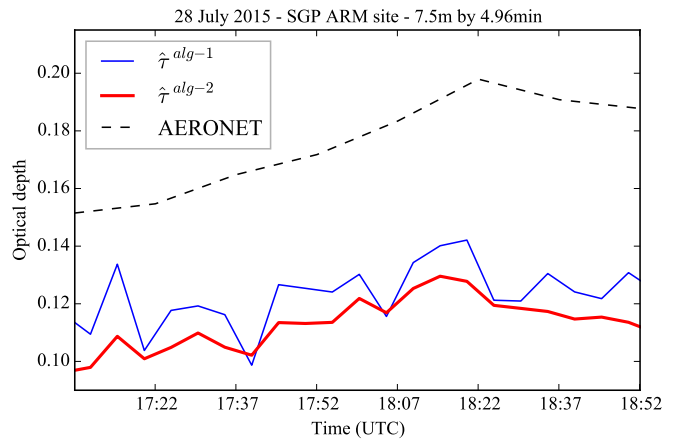


Figure 12: The optical depth values inverted with the new $\hat{\tau}^{alg-2}$ and standard $\hat{\tau}^{alg-1}$ approaches are compared against that of AERONET. This image shows that the optical depth inverted with the new approach agrees with the standard approach, and differ with the AERONET retrievals by a factor of less than 1.8. The difference between the HSRL and AERONET instrument optical depth values are due to uncertainties of geometric overlap function. Furthermore these two instruments do not exactly observe the same atmospheric columns.

6.3 Case study three - scatter cross-section of a cirrus cloud

In this case study the scatter cross-section of a dense cirrus cloud were inverted. The top image of Figure 13 shows the inverted scatter cross-section $\hat{\beta}^{alg-2}$ of the new approach, and the bottommost image is the inverted scatter cross-section $\hat{\beta}^{alg-1}$ of the standard approach. With the new approach the matrix B_l was set to $\mathbb{1}_{N \times K}$. And with the standard approach, a Savitzky-Golay lowpass filter was used for both the range and temporal axes [29]. The window-length of the range axis was set to 600m and for the temporal axis it was 600s. And for both axes, the polynomial order for the Savitzky-Golay filter was set to one. The resolution of data that were used was 7.5m by 1:52.5min (45 columns). The optical depth of the cloud is between 0.4 and 0.55, hence the inverted scatter cross-section above the cloud have larger uncertainties than the cross-sections in and below the cloud.

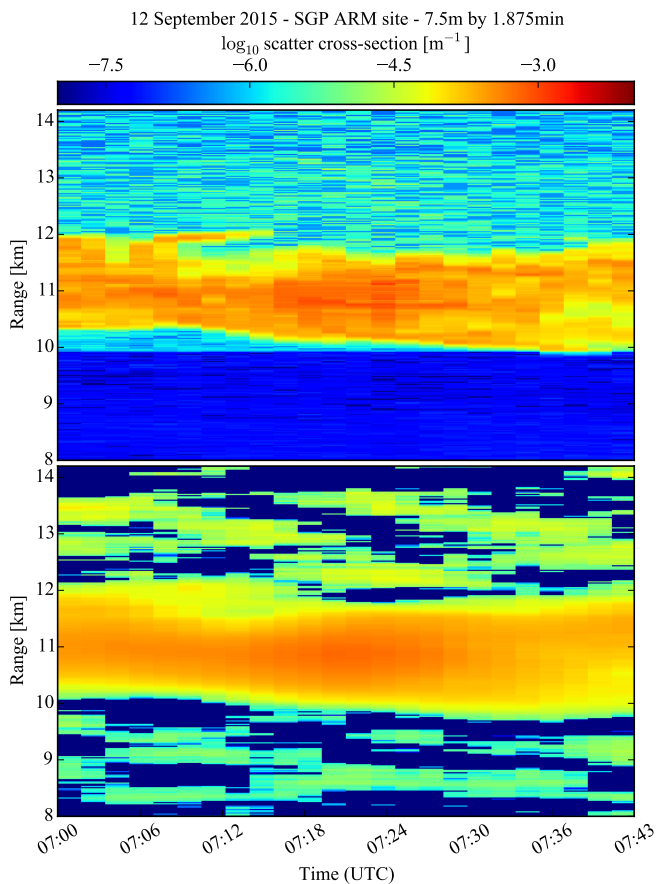


Figure 13: The two image show the inverted scatter cross-section of the new $\hat{\beta}^{alg-2}$ and standard $\hat{\beta}^{alg-1}$ approaches, where the topmost image corresponds to the new approach. Although the inverted cross-section $\hat{\beta}^{alg-2}$ do look considerably better than $\hat{\beta}^{alg-1}$, there are several artifacts such as at 10km at between 7:00 UTC and 7:23 UTC. We are yet to establish what the predominant source is of these artifacts.

Recall that Algorithm 2 estimates the scatter cross-section by first estimating for the lidar ratio, and that the lidar ratio has to be constrained to a closed subset of $[1, \infty)^{N \times K}$ so that the loss function is strictly convex; see §4.4. If a single lidar ratio is assumed for the whole scene, the maximum lidar ratio of the constraint set

is approximately 60. In other words, to guarantee that the Hessian matrix of the loss function is positive definite for a constant lidar ratio, the lidar ratio should be less than 60. For this case study we did set the lidar ratio upper bound to 600, and from the experiments that were conducted we observed that the estimation of the lidar ratios was numerically stable.

On a last note, for this case study only the molecular channel observations Y_m were used to estimate for the scatter cross-section, whereas in the the simulations both Y_c and Y_m were used. We found that any uncertainties in the inverted backscatter $\hat{\nu}^{alg-2}$ propagates through the inversion of the scatter cross-section. Since the calibration coefficient θ_m is very small (see §2.4), less uncertainty of the backscatter cross-section $\hat{\nu}^{alg-2}$ is introduced in $\hat{\beta}^{alg-2}$ when only the molecular channel is used.

6.3.1 Validation

The inverted lidar ratios are used to validate the estimated scatter cross-section. We validate the inverted lidar ratio of Algorithm 2 by comparing it against inverted lidar ratio of Algorithm 1, since there are no alternative data sources at our disposal (like AERONET) which we can use. The inverted lidar ratio values of Algorithms 2 and 1 should be in agreement, since a large number of columns are accumulated to increase the signal SNR.

In addition to the lidar ratio that are inverted with Algorithms 1 and 2, we also use the bulk lidar ratio to validate the inverted scatter cross-section; the bulk lidar ratio is defined in the following subsection. For both the lidar ratio and bulk lidar ratio, we only consider the region within the cloud. The cloud boundaries were determined using the inverted backscatter $\hat{\nu}^{alg-2}$ with a threshold of 10^{-6} . Hence, we are excluding the influence of multiple scattering outside the cloud.

Bulk lidar ratio

We define the bulk lidar ratio as ratio between the averaged inverted scatter and backscatter cross-sections, which are constrained to the inner part of the cloud. In other words, for a continuous region on a fixed column delineated by the top and bottom of the cloud, the inverted scatter and backscatter cross-sections are averaged and divided with each other. Since the bulk lidar ratio is ratio of two averaged quantities, it should be less noisy than the full waveform lidar ratio computed using Algorithms 1 and 2.

The topmost image of Figure 14 shows the bulk lidar ratio of the new and standard approaches. The bottommost image shows the reciprocal of the bulk lidar ratio, which is the bulk 180° phase function. The difference between the lidar ratios of the different approaches are within ± 5 . Furthermore, the lidar ratio are within the range of lidar ratios of Figure 3.3 of [28, §3.3].

Full waveform lidar ratio

The top left image of Figure 15 shows a single column of the inverted lidar ratio of the new $\hat{\mu}^{alg-2}$ and standard $\hat{\mu}^{alg-1}$ approaches. The top right image is the corresponding backscatter cross-section of the different approaches. The bottommost image is the average lidar ratio over the different columns, where each average was calculated within the cloud.

Although the lidar ratio $\hat{\mu}^{alg-2}$ appears to be “blocky”, it does follow the upper and downward trends of $\hat{\mu}^{alg-1}$. Recall from §4.1 that the TV-PMLE implicitly constrains the lidar ratio to be piecewise constant. Hence, in a low SNR image, any variation of the lidar ratio will be approximated with block shaped curves.

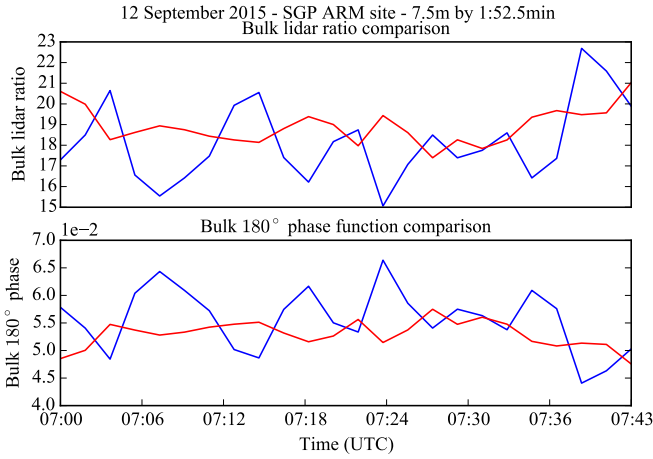


Figure 14: This figure corresponds to Figure 13; it demonstrates that the bulk lidar ratio of the new $\hat{\mu}^{alg-2}$ and standard $\hat{\mu}^{alg-1}$ approaches agrees with each other within a difference of ± 5 . The bulk lidar ratio is the ratio between the averaged inverted scatter and backscatter cross-sections in the cloud region. The topmost image shows the bulk lidar ratio of the new approach and the standard approach. The bottommost image shows the reciprocal of the bulk lidar ratio, which is the bulk 180° backscatter phase function.

Furthermore, uncertainty in the inverted backscatter cross-section $\hat{\nu}^{alg-2}$ potentially contribute to the uncertainties in $\hat{\mu}^{alg-2}$. In fact, although it is not clearly visible in the top right image of Figure 15, the inverted backscatter cross-section $\hat{\nu}^{alg-2}$ are potentially slightly biased. This is due to the piecewise constant approximation of the scaled attenuated backscatter (see §4.2.1). We plan to circumvent this issue in our future research.

6.4 Case study four - scatter cross-section of a cirrus cloud

A less dense cirrus cloud is used in this case study, compared to the case study three §6.3. The topmost image of Figure 16 shows the inverted scatter cross-section $\hat{\beta}^{alg-2}$ of the new approach. And the bottommost image show the inverted scatter cross-section $\hat{\beta}^{alg-1}$ of the standard approach. With the new approach the matrix B_i was set to $\mathbb{1}_{N \times K}$. And with the standard approach, a Savitzky-Golay lowpass filter was used for both the range and temporal axes [29]. The window-length of the range axis was set to 600m and for the temporal axis it was 600s. And for both axes, the polynomial order for the Savitzky-Golay filter was set to one. As with case study three, we use the bulk lidar ratio and the lidar ratio to validate the inverted scatter cross-section.

Recall that with Algorithm 2 the lidar ratio has to be constrained to a closed subset of $[1, \infty)^{N \times K}$, so that the loss function is strictly convex; see §4.4. If a single lidar ratio is assumed for the whole scene, the maximum lidar ratio of the constraint set is approximately 100. In other words, to guarantee that the Hessian matrix of the loss function is positive definite for a constant lidar ratio, the lidar ratio should be less than 100. For this case study we did set the lidar ratio upper bound to 200, and from the experiments that were conducted we observed that the estimation of the lidar ratios was numerically stable.

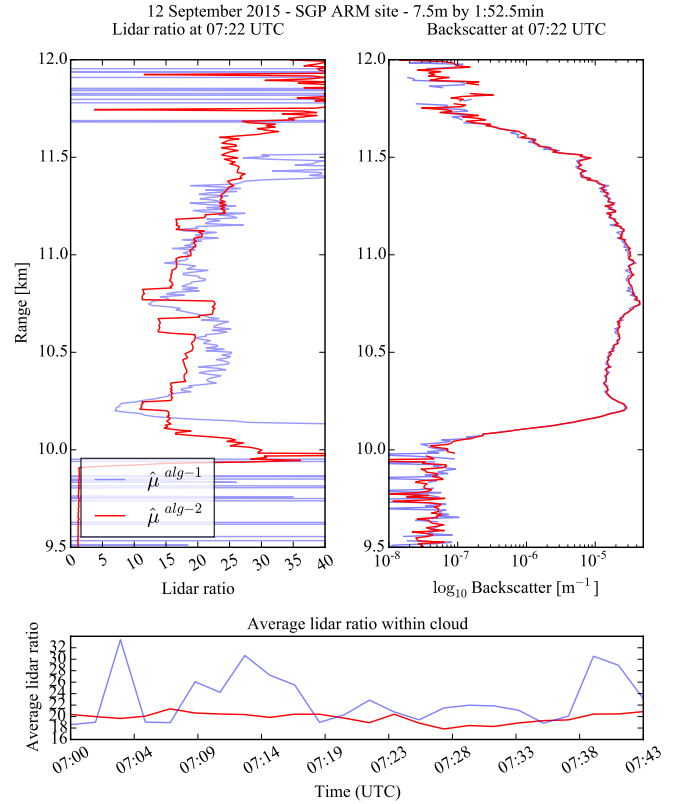


Figure 15: This figure corresponds to Figure 13. The top left image shows a single column of the inverted lidar ratios of the new $\hat{\mu}^{alg-2}$ and the standard $\hat{\mu}^{alg-1}$ approaches. The top right image shows the corresponding inverted backscatter cross-sections of the new and standard approaches. The bottommost image show the average lidar ratios horizontally across the cloud, where the each average was calculated within the cloud. The bottommost image shows that the lidar ratios of the new and standard approaches are similar.

6.4.1 Validation

Bulk lidar ratio

The topmost image of Figure 17 shows the bulk lidar ratio of the new and standard approaches. Refer to §6.3.1 for the definition of the bulk lidar ratio quantity. The cloud bottom and top boundaries were determined using the inverted backscatter cross-section $\hat{\nu}^{alg-2}$ with a threshold of 3×10^{-7} . The difference between the new and standard approach bulk lidar ratios are within ± 10 . There are larger uncertainties in the inverted bulk lidar ratios compared to case study three, since the backscatter cross-section of the cloud is less than 10^{-5} . Apart from this, there is agreement between the bulk lidar ratios in regards with upward and downward trends. The bottommost image shows the reciprocal of the bulk lidar ratio, which is the bulk 180° backscatter phase function.

Full waveform lidar ratio

The top left image of Figure 18 shows a single column of the inverted lidar ratio of the new $\hat{\mu}^{alg-2}$ and standard $\hat{\mu}^{alg-1}$ approaches. The top right image is the corresponding backscatter cross-sections of the different approaches. The bottommost image

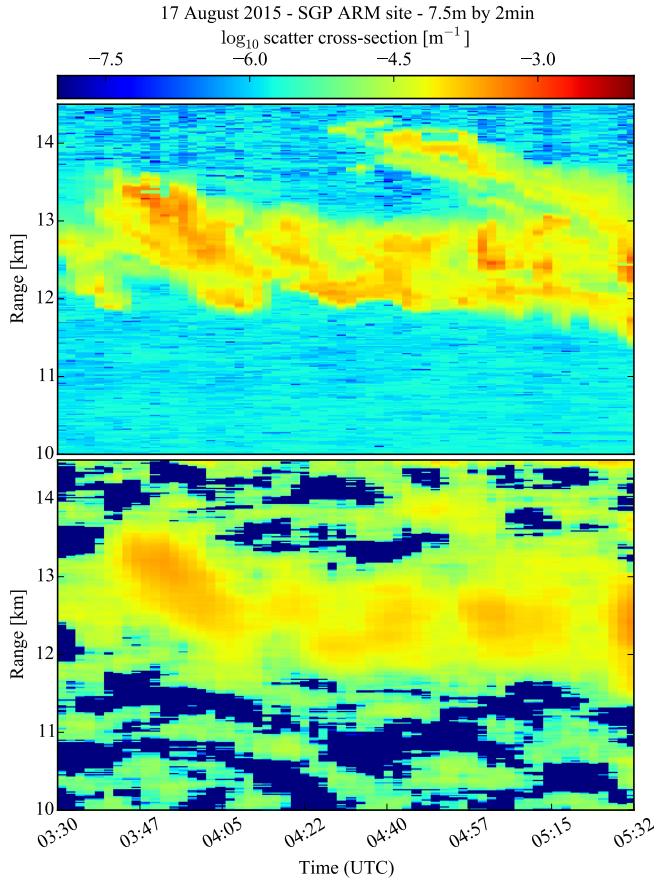


Figure 16: The two images show the inverted scatter cross-section of the new $\hat{\beta}^{alg-2}$ and standard $\hat{\beta}^{alg-1}$ approaches, where the topmost image corresponds to the new approach. The scatter cross-section below the cloud in this case is larger than in case three (see Figure 13), although the backscatter cross-sections are in the order of 3×10^{-8} . A potential contributor to this issue is uncertainty in the geometric overlap function.

is the average lidar ratio of the different columns, where each average was calculated within the cloud. As it was mentioned in §6.3, the lidar ratio in the top left image appears to be “blocky”, since the lidar ratio coefficients are implicitly approximated by piecewise constant functions. The bottommost image shows that the average lidar ratio are alike, though the average inverted lidar ratio $\hat{\mu}^{alg-1}$ appears to be more noisy.

The inverted lidar ratios in Figure 18 is interesting, in the sense that the lidar ratios differ as a function of range in correspondence with the depolarization coefficients of the cloud. In other words, there is a slight correlation between the depolarization and lidar ratios. The topmost image of Figure 19 shows the inverted backscatter cross-section $\hat{\tau}^{alg-2}$ of Figure 18 and the linear depolarization coefficients are shown in the bottommost image. At 4:34 UTC the linear depolarization varies between approximately 0.3 and 0.6. In the top left image of Figure 18 we observe that the lidar ratio changes as a function of the linear depolarization. For example the lidar ratios between 12.6km and 13km differ from those between 12km and 12.6km. The lidar ratios at 13.6km and 14.2km are mixed with clear-sky observations, hence do not purely represent lidar ratios of clouds.

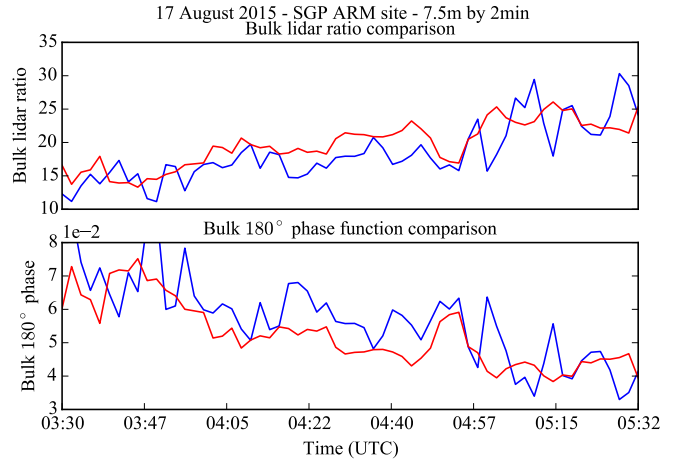


Figure 17: This figure corresponds to Figure 16; it demonstrates that the bulk lidar ratios of the new $\hat{\mu}^{alg-2}$ and standard $\hat{\mu}^{alg-1}$ approaches agrees with each other within a difference of ± 10 . The topmost image shows the bulk lidar ratios of the new approach and the standard approach. The bulk lidar ratio is the ratio between the averaged inverted scatter and backscatter cross-sections in the cloud region. The bottommost image shows the reciprocal of the bulk lidar ratio, which is the bulk 180° backscatter phase function.

7 Conclusion and future work

We presented a new approach to invert backscatter and scatter cross-sections from photon-counting HSRL observations. Considerably better estimates - smaller errors - of the backscatter and scatter cross-sections can be obtained with the TV-PMLE estimators (see §4) compared to the standard approach (see §3), as it was demonstrated in §5 and §6. The improved results, like that of Figure 16, are due to the fact that the new estimators take in account the noise model and the estimators impose a smoothness constraint on the estimates.

The advantage of using a TV-PMLE is that smoothness constraint is imposed on a whole image, whereas with block averaging a smoothness constraint is set on individual blocks independent from each other. In addition to taking the noise physical model in account, the TV-PMLE utilizes the spatial information of the noisy observations, whereas the standard approach does not. We deduce that the SNR required by the algorithms that are presented in this paper is less than the standard approach, in order to obtain a more accurate estimate (smaller MSE) of either the scatter and backscatter cross-sections. This assertion is based on the results presented in sections §5 and §6.

In addition to further validate our algorithms, our long term goals are to expand our work so that it will be applicable to 1) single channel lidar systems and 2) analog-mode lidar systems and 3) space-based lidar systems. With single-channel lidar systems further constraint have to be imposed so that meaningful inverted backscatter and scatter cross-sections can be obtained. Further research will be required to determine what appropriate constraints can be imposed, and how it can be imposed. With analog-mode lidar systems, the research challenge will be to derive or approximate the MLE for Compounded Poisson noise [7]; this noise differ significantly from Gaussian and Poisson noise. Once the technique has been adapted for single channel lidar and Compounded Poisson noise, the technique has the potential to

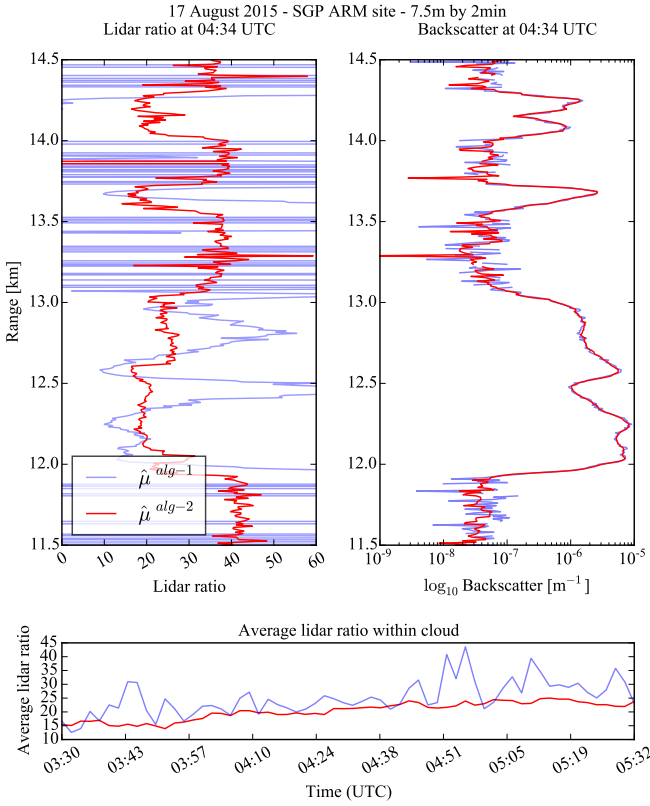


Figure 18: This figure corresponds to Figure 16. The top left image shows a single column of the inverted lidar ratios of the new $\hat{\mu}^{alg-2}$ and the standard $\hat{\mu}^{alg-1}$ approaches. The top right image shows the corresponding inverted backscatter cross-sections of the new and standard approaches. The bottommost image shows the average lidar ratios horizontally across the cloud, where the each average was calculated within the cloud. The bottommost image shows that the lidar ratios of the new and standard approaches are similar.

greatly improve current systems such as CATS and the ten year record of CALIPSO observations [39, 1].

APPENDIX

A Thinning a Poisson distributed matrix in creating the training and testing matrices

Without loss of generality, suppose Y be a Poisson random variable where each entry is independent from each other and $\mathbb{E}_Y[Y] = \lambda$. And for a given Y , let Z be a Binomial random variable, where $\mathbb{E}_{Z|Y}[Z|Y = y] = yp$ and $p \in (0, 1)$. The random variables Y and Z are independent from each other. It can be proved that Z is Poisson distributed with $\mathbb{E}_{Z,Y}[Z] = \mathbb{E}_Y[\mathbb{E}_{Z|Y}[Z|Y]] = p\lambda$, where the expectation is taken over the PMFs of both Y and Z .

Now suppose Y_i is Poisson distributed random matrix. Using the procedure described in the previous paragraph, we can create a “training” matrix Y_i^{trn} where $\mathbb{E}[Y_i^{trn}] = p\mathbb{E}[Y_i]$. The “testing” matrix Y_i^{tst} is created by the removing Y_i^{trn} from Y_i . This is achieved by subtracting the two matrices.

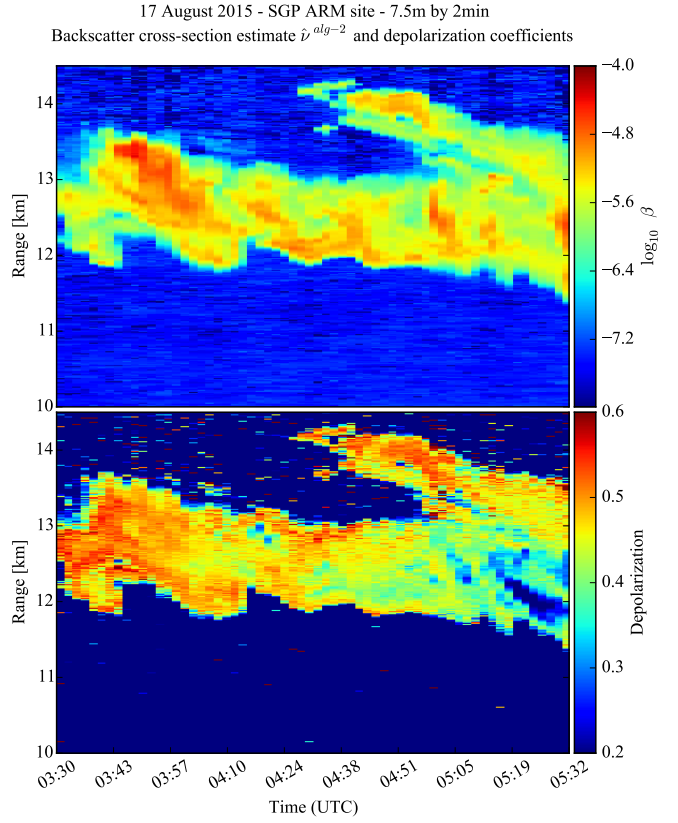


Figure 19: This figure corresponds to Figure 16. The top image shows the inverted backscatter cross-section of the Algorithm 2. The bottom image shows the linear depolarization measurements, indicating that the cloud consisted of a mix of different ice crystal types. From these two images we deduce that cloud in Figure 16 consists of various ice crystal types, and in Figure 18 we can observe a slight correlation between the depolarization and lidar ratios.

B Proof of Theorem 1

Define the event

$$\mathcal{A}_{i,n} = \left\{ e_n^T [g_i(\mu; \hat{\nu})]^2 > e_n^T [Y_i \cdot b_i] \right\}. \quad (57)$$

The probability that the Hessian matrix $H_i(\mu)$ is positive definite, is equal to the probability of the event $\cap_{n=1}^N \mathcal{A}_{i,n}$. To prove Theorem 1 we breakup the proof in several lemmas. The purpose of each of the following lemmas are:

Lemma 2: A concentration inequality of a Poisson random variable is given. This is required to find a probabilistic lower bound for Theorem 1.

Lemma 3: A lower bound is proven of the probability $\mathbb{P}(\mathcal{A}_{i,n})$.

Lemma 4: A lower bound of $\mathbb{P}(\cap_{n=1}^N \mathcal{A}_{i,n})$ is proven.

Lemma 5: Lemmas 2, 3 and 4 are put together to prove Theorem 1.

Lemma 2. Let Y be a Poisson random variable and $\epsilon > 0$. The Chernoff

bound of Y is

$$\log_e \mathbb{P}(Y \geq (1 + \epsilon)\mathbb{E}[Y]) \quad (58)$$

$$\leq -\mathbb{E}[Y] [(1 + \epsilon) \log_e(1 + \epsilon) - \epsilon] \quad (59)$$

$$\leq -\mathbb{E}[Y] \left(\frac{\epsilon^2}{2 + 1.5\epsilon} \right). \quad (60)$$

Proof. The first upper bound is straightforward to compute by using the Chernoff bound technique [40, §4.5]. Refer to Lemma 2.4 of [41] to see a proof of the second upper bound. \square

Lemma 3. Let \hat{v} be given and let Y_l be a Poisson random vector such that $\mathbb{E}[Y_l] = S_l$. Define

$$\tilde{\zeta}(n) = e_n^T S_l \frac{\tilde{\epsilon}^2(n)}{2 + 1.5\tilde{\epsilon}(n)} \quad (61)$$

$$\tilde{\epsilon}(n) = -1 + e_n^T \frac{[g_l(\mu; \hat{v})]^2}{b_l \cdot S_l}. \quad (62)$$

Then

$$\log_e \mathbb{P}(\mathcal{A}_{l,n}^c) = \log_e \mathbb{P}(e_n^T Y_l \geq (1 + \tilde{\epsilon}(n))e_n^T S_l) \quad (63)$$

$$\leq -\tilde{\zeta}(n). \quad (64)$$

Proof. We have that

$$\mathcal{A}_{l,n}^c = \left\{ e_n^T \frac{[g_l(\mu; \hat{v})]^2}{b_l} \leq e_n^T Y_l \right\} \quad (65)$$

$$= \left\{ e_n^T Y_l \geq (1 + \tilde{\epsilon}(n))e_n^T S_l \right\}. \quad (66)$$

Invoking Lemma 2 we get

$$\log_e \mathbb{P}(\mathcal{A}_{l,n}^c) \leq -\tilde{\zeta}(n), \quad (67)$$

which completes the proof. \square

Lemma 4. Let \hat{v} be given. The probability that the Hessian matrix (37) is positive definite is lower bounded by

$$\mathbb{P} \left[\bigcap_{n=1}^N \mathcal{A}_{l,n} \right] \geq 1 - \sum_{n=1}^N \exp[-\tilde{\zeta}(n)]. \quad (68)$$

Proof. If we find an upper bound for $\mathbb{P} \left[\bigcup_{n=1}^N \mathcal{A}_{l,n}^c \right]$, then we are done with the proof, since $\mathbb{P} \left[\bigcap_{n=1}^N \mathcal{A}_{l,n} \right] = 1 - \mathbb{P} \left[\bigcup_{n=1}^N \mathcal{A}_{l,n}^c \right]$. We have that

$$\mathbb{P} \left[\bigcup_{n=1}^N \mathcal{A}_{l,n}^c \right] \leq \sum_{n=1}^N \mathbb{P}(\mathcal{A}_{l,n}^c) \quad (69)$$

$$\leq \sum_{n=1}^N \exp[-\tilde{\zeta}(n)], \quad (70)$$

where the first inequality we used the union bound inequality (see [40, §1]) and the second inequality is from Lemma 3. \square

Lemma 5. Let \hat{v} be given. Let Y_l be a Poisson random vector such that $\mathbb{E}[Y_l] = S_l$, and the corresponding denoised estimate is $\hat{S}_l = f_l(\hat{\omega}_l)$. Suppose an oracle tells us that

$$\frac{e_n^T \hat{S}_l}{\delta_U} \leq e_n^T S_l \leq \frac{e_n^T \hat{S}_l}{\delta_L}. \quad (71)$$

Then

$$\mathbb{P} \left[\bigcap_{n=1}^N \mathcal{A}_{l,n} \right] \geq 1 - \sum_{n=1}^N \exp[-\tilde{\zeta}(n)], \quad (72)$$

where

$$\tilde{\zeta}(n) = \frac{e_n^T \hat{S}_l}{\delta_U} \frac{\epsilon^2(n)}{2 + 1.5\epsilon(n)} \quad (73)$$

$$\epsilon(n) = -1 + \delta_L e_n^T \left(\frac{[g_l(\mu; \hat{v})]^2}{b_l \cdot \hat{S}_l} \right) \quad (74)$$

and with the condition that for all $n \geq N$

$$e_n^T g_l(\mu; \hat{v}) > e_n^T \sqrt{\frac{b_l \cdot \hat{S}_l}{\delta_L}}. \quad (75)$$

Proof. We want to relax the lower bound given in Lemma 4 by using the inequality (71). We do this by finding a function which is smaller than $\tilde{\zeta}(n)$. If $\tilde{\epsilon}(n) > 0$, the coefficient $\tilde{\zeta}(n)$ monotonically increases as $\tilde{\epsilon}(n)$ increases. To prove this assertion, let

$$q(\tilde{\epsilon}(n)) = \frac{\tilde{\epsilon}(n)^2}{2 + 1.5\tilde{\epsilon}(n)}. \quad (76)$$

The first derivative of $q(\tilde{\epsilon}(n))$ is

$$q^{(1)}(\tilde{\epsilon}(n)) = \frac{1.5\tilde{\epsilon}^2(n) + 4\tilde{\epsilon}(n)}{[1.5\tilde{\epsilon}(n) + 2]^2}, \quad (77)$$

which is strictly positive if $\tilde{\epsilon}(n) > 0$. To ensure that $\tilde{\epsilon}(n) > 0$, we require that

$$e_n^T g_l(\mu; \hat{v}) > e_n^T \sqrt{\frac{b_l \cdot \hat{S}_l}{\delta_L}} \geq e_n^T \sqrt{b_l \cdot S_l}. \quad (78)$$

With the condition (78), we have that $\epsilon(n) \leq \tilde{\epsilon}(n)$ and

$$\tilde{\zeta}(n) \geq e_n^T \frac{\hat{S}_l}{\delta_U} \frac{\epsilon^2(n)}{2 + 1.5\tilde{\epsilon}(n)} \geq \zeta(n). \quad (79)$$

To conclude the proof with the assertion that

$$\mathbb{P} \left[\bigcap_{n=1}^N \mathcal{A}_{l,n} \right] \geq 1 - \sum_{n=1}^N \exp[-\tilde{\zeta}(n)] \geq 1 - \sum_{n=1}^N \exp[-\zeta(n)]. \quad (80)$$

\square

Acknowledgments

The authors would like to thank Zachary Harmany and Albert Oh for sharing their most recent source code of [14]. We thank Rick Wagener for maintaining the AERONET instruments and making the data available at the SGP ARM site. We also thank Ilya Razenkov, Joe Garcia and Martin Lawson for their dedicated hard work in maintaining and developing the Wisconsin-Madison HSRL system.

References

- [1] D. M. Winker, M. A. Vaughan, A. Omar, Y. Hu, K. A. Powell, Z. Liu, W. H. Hunt, and S. A. Young, "Overview of the CALIPSO mission and CALIOP data processing algorithms," *Journal of Atmospheric and Oceanic Technology*, vol. 26, no. 11, pp. 2310–2323, 2009.
- [2] J. W. Hair, C. A. Hostetler, A. L. Cook, D. B. Harper, R. A. Ferrare, T. L. Mack, W. Welch, L. R. Izquierdo, and F. E. Hovis, "Airborne high spectral resolution lidar for profiling aerosol optical properties," *Applied Optics*, vol. 47, no. 36, pp. 6734–6752, 2008.

- [3] Y. Durand, A. Hélière, J. Bézy, and R. Meynard, "The ESA EarthCARE mission: results of the ATLID instrument pre-developments," in *Proc. SPIE*, vol. 6750, 2007, p. 675015.
- [4] M. McGill, D. Hlavka, W. Hart, V. S. Scott, J. Spinhirne, and B. Schmid, "Cloud physics lidar: Instrument description and initial measurement results," *Applied Optics*, vol. 41, no. 18, pp. 3725–3734, 2002.
- [5] E. J. Welton, J. R. Campbell, J. D. Spinhirne, and V. S. Scott III, "Global monitoring of clouds and aerosols using a network of micropulse lidar systems," in *Second International Asia-Pacific Symposium on Remote Sensing of the Atmosphere, Environment, and Space*. International Society for Optics and Photonics, 2001, pp. 151–158.
- [6] Z. Liu, W. Hunt, M. Vaughan, C. Hostetler, M. McGill, K. Powell, D. Winker, and Y. Hu, "Estimating random errors due to shot noise in backscatter lidar observations," *Applied optics*, vol. 45, no. 18, pp. 4437–4447, 2006.
- [7] Z. Liu and N. Sugimoto, "Simulation study for cloud detection with space lidars by use of analog detection photomultiplier tubes," *Applied optics*, vol. 41, no. 9, pp. 1750–1759, 2002.
- [8] T. Hastie, R. Tibshirani, and J. Friedman, *The Elements of Statistical Learning: Data Mining, Inference, and Prediction*, 2nd ed., ser. Springer Series in Statistics. Springer New York, 2009.
- [9] C. D. Rodgers, *Inverse methods for atmospheric sounding: theory and practice*. World scientific Singapore, 2000, vol. 2.
- [10] E. Eloranta, "High Spectral Resolution Lidar Measurements of Atmospheric Extinction: Progress and Challenges," in *Aerospace Conference, 2014 IEEE*. IEEE, 2014, pp. 1–6.
- [11] T. Nishizawa, N. Sugimoto, I. Matsui, A. Shimizu, B. Tatarov, and H. Okamoto, "Algorithm to retrieve aerosol optical properties from high-spectral-resolution lidar and polarization mie-scattering lidar measurements," *Geoscience and Remote Sensing, IEEE Transactions on*, vol. 46, no. 12, pp. 4094–4103, 2008.
- [12] S. A. Young, D. Winker, M. Vaughan, Y. Hu, and R. Kuehn, "CALIOP Algorithm Theoretical Basis Document, Part 4: Extinction retrieval algorithms," NASA Langley Research Center, Tech. Rep., 2008.
- [13] A. Ansmann, U. Wandinger, O. Le Rille, D. Lajas, and A. G. Straume, "Particle backscatter and extinction profiling with the spaceborne high-spectral-resolution Doppler lidar ALADIN: methodology and simulations," *Applied optics*, vol. 46, no. 26, pp. 6606–6622, 2007.
- [14] A. Oh, Z. Harmany, and R. Willett, "Logarithmic total variation regularization for cross-validation in photon-limited imaging," in *Image Processing (ICIP), 2013 20th IEEE International Conference on*, Sept 2013, pp. 484–488.
- [15] Z. T. Harmany, R. F. Marcia, and R. M. Willett, "This is SPIRAL-TAP: Sparse Poisson Intensity Reconstruction Algorithms—Theory and Practice," *Image Processing, IEEE Transactions on*, vol. 21, no. 3, pp. 1084–1096, 2012.
- [16] R. M. Willett and R. D. Nowak, "Platelets: a multiscale approach for recovering edges and surfaces in photon-limited medical imaging," *Medical Imaging, IEEE Transactions on*, vol. 22, no. 3, pp. 332–350, 2003.
- [17] G. W. Petty, *A first course in atmospheric radiation*. Sundog Pub, 2006.
- [18] E. Eloranta. (2014, 10) <http://hsrl.ssec.wisc.edu>. [Online]. Available: <http://hsrl.ssec.wisc.edu>
- [19] P. Yang, Y. X. Hu, D. M. Winker, J. Zhao, C. A. Hostetler, L. Poole, B. A. Baum, M. I. Mishchenko, and J. Reichardt, "Enhanced lidar backscattering by quasi-horizontally oriented ice crystal plates in cirrus clouds," *Journal of Quantitative Spectroscopy and Radiative Transfer*, vol. 79, pp. 1139–1157, 2003.
- [20] C. A. Hostetler, Z. Liu, J. Reagan, M. Vaughan, D. Winker, M. Osborn, W. Hunt, K. Powell, and C. Trepte, "CALIOP Algorithm Theoretical Basis Document—Part 1: Calibration and Level 1 Data Products," *Doc. PC-SCI*, vol. 201, 2006.
- [21] S. Chandrasekhar, *Radiative Transfer*, ser. Dover Books on Intermediate and Advanced Mathematics. Dover Publications, 1960.
- [22] R. Measures, *Laser Remote Sensing: Fundamentals and Applications*, ser. Wiley-Interscience publication. John Wiley & Sons, 1984.
- [23] R. M. Measures, *Laser remote chemical analysis*, ser. Chemical analysis. New York : Wiley, 1988, "A Wiley-Interscience publication."
- [24] E. E. Eloranta, *High spectral resolution lidar*. Springer, 2005.
- [25] R. M. Willett and R. D. Nowak, "Multiscale poisson intensity and density estimation," *Information Theory, IEEE Transactions on*, vol. 53, no. 9, pp. 3171–3187, 2007.
- [26] P. P. B. Eggermont, V. N. LaRiccia, and V. LaRiccia, *Maximum penalized likelihood estimation*. Springer, 2001, vol. 1.
- [27] I. Razenkov, "Characterization of a Geiger-mode Avalanche Photodiode Detector for High Spectral Resolution Lidar," Ph.D. dissertation, University of Wisconsin-Madison, 2010.
- [28] R. E. Holz, "Measurements of cirrus backscatter phase functions using a high spectral resolution lidar," Master's thesis, University of Wisconsin-Madison, 2002.
- [29] R. W. Schafer, "On the Frequency-Domain Properties of Savitzky-Golay Filters," in *Proc. 2011 DSP/SPE Workshop*, 2010, pp. 54–59.
- [30] P. Pornsawad, G. D'Amico, C. Böckmann, A. Amodeo, and G. Pappalardo, "Retrieval of aerosol extinction coefficient profiles from Raman lidar data by inversion method," *Applied Optics*, vol. 51, no. 12, pp. 2035–2044, 2012.
- [31] P. Tian, X. Cao, J. Liang, L. Zhang, N. Yi, L. Wang, and X. Cheng, "Improved empirical mode decomposition based denoising method for lidar signals," *Optics Communications*, vol. 325, pp. 54–59, 2014.
- [32] Cimel. (2016, 2) http://support.cimel.fr/photo/pdf/ce370_us.pdf. [Online]. Available: http://support.cimel.fr/photo/pdf/ce370_us.pdf

- [33] F. O’Sullivan, “A statistical perspective on ill-posed inverse problems,” *Statistical science*, pp. 502–518, 1986.
- [34] D. Needell and R. Ward, “Stable image reconstruction using total variation minimization,” *SIAM Journal on Imaging Sciences*, vol. 6, no. 2, pp. 1035–1058, 2013.
- [35] S. J. Wright, R. D. Nowak, and M. A. Figueiredo, “Sparse Reconstruction by Separable Approximation,” *Signal Processing, IEEE Transactions on*, vol. 57, no. 7, pp. 2479–2493, 2009.
- [36] J. Nocedal and S. Wright, *Numerical optimization*. Springer Science & Business Media, 2006.
- [37] A. Beck and M. Teboulle, “Fast Gradient-Based Algorithms for Constrained Total Variation Image Denoising and Deblurring Problems,” *Image Processing, IEEE Transactions on*, vol. 18, no. 11, pp. 2419–2434, 2009.
- [38] B. Holben, T. Eck, I. Slutsker, D. Tanre, J. Buis, A. Setzer, E. Vermote, J. Reagan, Y. Kaufman, T. Nakajima *et al.*, “AERONET - A federated instrument network and data archive for aerosol characterization,” *Remote sensing of environment*, vol. 66, no. 1, pp. 1–16, 1998.
- [39] M. McGill, E. Welton, J. Yorks, and V. S. Scott, “CATS: A new earth science capability,” *Newsletter*, May June 2012.
- [40] J. Gubner, *Probability and Random Processes for Electrical and Computer Engineers*. Cambridge University Press, 2006.
- [41] C. McDiarmid, “Concentration,” in *Probabilistic methods for algorithmic discrete mathematics*. Springer, 1998, pp. 195–248.